

# Improved Stencil Selection for Meshless Finite Difference Methods in 3D

Oleg Davydov\*, Dang Thi Oanh† and Ngo Manh Tuong‡

February 15, 2022

## Abstract

We introduce a geometric stencil selection algorithm for Laplacian in 3D that significantly improves octant-based selection considered earlier. The goal of the algorithm is to choose a small subset from a set of irregular points surrounding a given point that admits an accurate numerical differentiation formula. The subset serves as an influence set for the numerical approximation of the Laplacian in meshless finite difference methods using either polynomial or kernel-based techniques. Numerical experiments demonstrate a competitive performance of this method in comparison to the finite element method and to other selection methods for solving the Dirichlet problems for the Poisson equation on several STL models. Discretization nodes for these domains are obtained either by 3D triangulations or from Cartesian grids or Halton quasi-random sequences.

**Keyword.** *RBF-FD, meshless finite difference method, generalized finite differences*  
*2010 AMS Subject Classification.* 65M06, 65N06

## 1 Introduction

We consider the Dirichlet problem for the Poisson equation: Find a function  $u : \overline{\Omega} \rightarrow \mathbb{R}$  such that

$$\begin{aligned} \Delta u &= f & \text{in } \Omega, \\ u &= g & \text{on } \partial\Omega. \end{aligned} \tag{1}$$

where  $\Delta$  is the Laplacian operator,  $\Omega \subset \mathbb{R}^3$  a domain,  $f$  a real-valued function defined in  $\Omega$ , and  $g$  a real-valued function defined on  $\partial\Omega$ .

Meshless finite difference methods for (1) are defined as follows. Let  $\Xi$  be a finite set of discretization nodes, where  $\Xi \subset \overline{\Omega}$ , and  $\Xi_{\text{int}} := \Xi \cap \Omega$ ,  $\partial\Xi := \Xi \cap \partial\Omega$ . For each  $\zeta \in \Xi_{\text{int}}$ , choose a *set of influence*  $\Xi_\zeta := \{\xi_1, \xi_2, \dots, \xi_k\} \subset \Xi$  with  $\xi_1 = \zeta$ , and approximate  $\Delta u(\zeta)$  by a numerical differentiation formula

$$\Delta u(\zeta) \approx \sum_{\xi \in \Xi_\zeta} w_{\zeta, \xi} u(\xi), \quad \zeta \in \Xi_{\text{int}}. \tag{2}$$

---

\*Department of Mathematics, University of Giessen, Arndtstrasse 2, 35392 Giessen, Germany, [oleg.davydov@math.uni-giessen.de](mailto:oleg.davydov@math.uni-giessen.de).

†Information Technology Department, Ministry of Education and training, 35 Dai Co Viet, Hai Ba Trung District, Hanoi, Vietnam, [dtoanh@moet.gov.vn](mailto:dtoanh@moet.gov.vn); [dtoanh@ictu.edu.vn](mailto:dtoanh@ictu.edu.vn). The work of this author was supported by a Natural Science Research Project of the Ministry of Education and Training under grant number B2019-TNA-03.T.

‡Department of Basic Sciences, Thai Nguyen University of Information & Communication Technology, Quyet Thang Ward, Thai Nguyen City, Vietnam, [nmtuong@ictu.edu.vn](mailto:nmtuong@ictu.edu.vn).

Thus, in contrast to the classical Finite Difference Method, *stencils* defined by the sets of influence and corresponding numerical differentiation weights  $w_{\zeta,\xi}$  are chosen individually for each node  $\zeta$ , rather than obtained by a simple scaling of one and the same stencil. This removes the need for a grid structure in  $\Xi$  and hence allows a meshless method.

The discretization of the problem (1) is given by the square linear system

$$\begin{aligned} \sum_{\xi \in \Xi_\zeta} w_{\zeta,\xi} \hat{u}_\xi &= f(\zeta), \quad \zeta \in \Xi_{\text{int}}; \\ \hat{u}_\xi &= g(\xi), \quad \xi \in \partial\Xi. \end{aligned} \quad (3)$$

By solving the system (3) we obtain a vector  $[\hat{u}_\xi]_{\xi \in \Xi}$  that serves as an approximation of the solution  $u$  of (1) at all nodes  $\xi \in \Xi$ .

A major motivation for meshless methods is that no connection information between nodes in  $\Xi$  is needed, which simplifies the task of *node generation* in comparison to *mesh generation*, where the nodes are connected into grid structures or elements that have to meet strict quality criteria. Obtaining good meshes needed in mesh-based methods is often notoriously difficult in applications, especially when  $\Omega$  is defined by a complicated CAD model, or when the mesh has to be quickly adapted to moving boundaries or singularities of the solution evolving in time.

Any particular meshless finite difference (mFD) method is defined by specific *stencil selection algorithm* for choosing the sets of influence  $\Xi_\zeta \subset \Xi$ ,  $\zeta \in \Xi_{\text{int}}$ , as well as an algorithm for computing numerical differentiation weights  $w_{\zeta,\xi}$ ,  $\zeta \in \Xi_{\text{int}}$ ,  $\xi \in \Xi_\zeta$ . The weights can be found by the traditional technique of requiring exactness of the formula (2) for polynomials of certain degree, as e.g. in [17], or by a radial basis function method (RBF-FD), see e.g. [13] and references therein. The accuracy of numerical differentiation formulas on irregular points obtained by various methods has been investigated in [9, 10, 11, 5].

The density of the linear system (3) is determined by the size  $k$  of the sets of influence  $\Xi_\zeta$  since the corresponding row of the system matrix has at most  $k$  nonzero entries. Since the density of the matrix is directly related to the cost of solving the resulting linear system, it is important to keep  $k$  as small as possible, even if more computation time is spent on selection. Indeed, the selection is done independently for each node  $\zeta$ , and therefore can be done in parallel without any complications, whereas the linear system may be very large for a large scale problem, so that higher sparsity is an important advantage.

In [6, 19] we developed adaptive meshless RBF-FD algorithms for solving elliptic equations with point singularities in 2D, with sets of influence consisting of just  $k = 7$  points, which delivers system matrices of about the same density as in the finite element method with linear shape functions. The accuracy of the solution is also similar to the finite element counterpart, while our method is purely meshless.

A general algorithm for the selection of sparse sets of influence based on the pivoted QR decomposition of the polynomial collocation matrices has been introduced in [4] and tested on elliptic interface problems in [8], showing convincing performance especially in the context of a high order polynomial-based mFD method.

In the recent paper [7] we investigated a simple method for selecting sets of influence in 3D that generalizes the well-known two-dimensional four-quadrant criterium of [18]. By selecting two points in each Cartesian octant centered at  $\zeta$ , we obtain  $\Xi_\zeta$  with  $k = 17$ , which leads to only slightly denser system matrices than those arising in the 3D finite element method with linear shape functions.

In this paper we suggest an improvement of the selection algorithm of [7] and compare its numerical performance with several alternative approaches for the selection of sets of influence in the meshless finite difference method, as well as with the finite element method. Comparison is performed on Poisson equations with Dirichlet boundary conditions for the unit ball, with known exact solution, and for three non-convex STL models with homogeneous Dirichlet boundary conditions, where we rely on reference solutions obtained with the finite element method on fine triangulations. We consider several methods of node generation, including nodes obtained by mesh generation (MATLAB PDE Toolbox triangulations; non-optimized Delaunay triangulations by Gmsh) as well as Cartesian grids and Halton quasi-random points. The results indicate that the new method works well even on less regular nodes and competes successfully with the finite element method and alternative selection algorithms for mFD.

The paper is organized as follows. Section 2 presents the new selection algorithm, whereas Sections 3 and 4 briefly describe weight computation and alternative selection methods. Section 5 is devoted to numerical experiments, and Section 6 provides a short conclusion.

## 2 Improvement of octant-based selection

The goal of a selection algorithm is to obtain suitable influence sets  $\Xi_\zeta = \{\xi_1, \dots, \xi_k\} \subset \Xi$ ,  $\xi_1 = \zeta$ , with as small as possible  $k$ , without expectation that the node set  $\Xi$  is highly regular. The simplest selection algorithm builds  $\Xi_\zeta$  by using  $\zeta$  and its  $k - 1$  nearest nodes in  $\Xi$ . According to numerical experiments in [1], even on very nicely distributed nodes obtained by rather expensive node generation methods, the number of points in  $\Xi_\zeta$  has to be at least twice the dimension of polynomials of degree  $p$  in order to achieve convergence of the method (3) with order  $\mathcal{O}(h^p)$ , where  $h$  measures the spacing of the nodes. In 3D this approach requires  $k \geq 20$  if we pursue a method comparable in accuracy to the finite element method with linear shape functions whose convergence order is  $\mathcal{O}(h^2)$ .

We consider a selection algorithm as successful if (a) it produces  $\Xi_\zeta$  with  $k$  less or equal 20 on cheaply generated nodes obtained without node improvement by repulsion and similar techniques that lead to highly regular nodes as in [1], and (b) it shows similar accuracy to the finite element method with the same number of degrees of freedom. The octant-based selection algorithms of [7] have been successful in this sense on nodes produced as vertices of a triangulation generated by MATLAB PDE Toolbox. However, these nodes are rather nicely distributed and therefore do not fully demonstrate the advantages of a meshless method. As we will see in Section 5, simple octant-based selection of [7] often fails on less regular nodes. We suggest here an improvement of this method that works well on irregular nodes obtained from non-optimized Delaunay triangulations or by combining Cartesian or Halton nodes inside a 3D domain with some discretization of its boundary.

A “geometric” selection method, such as our 2D algorithms in [6, 19] seeks a compromise between two goals that the nodes  $\xi_i$  are distributed as evenly as possible around  $\zeta$  and in the same time as near to  $\zeta$  as possible. In the earlier versions of our octant-based algorithms [7] either  $n = 2$  closest neighboring nodes are chosen in each coordinate octant around the given node  $\zeta \in \Xi$  [7, Algorithm 1], or only one closest node is taken in each of 16 half-octants [7, Algorithm 2], leading again to 2 nodes in each octant, and  $k \leq 17$ . These algorithms are fast and their results are quite good for relatively nice

discretizations  $\Xi$ . However, the nodes selected by this method may still be poorly distributed around  $\zeta$ , or even contain clusters, while wide ranges of directions from  $\zeta$  may receive no nodes in  $\Xi_\zeta$  if  $\Xi$  is rather irregular.

In the new algorithm, in order to improve the angular distribution of  $\xi_i$  around  $\zeta$ , we first select a larger number  $n > 2$  of candidate nodes in each of the eight octants. This produces a cloud of neighbors that better cover all directions from  $\zeta$ , but are too many, for example up to 24 in the case  $n = 3$ . Then, in the second stage of the algorithm, we go over these candidate nodes and choose at most  $k - 1$  of them to include in the final set of influence  $\Xi_\zeta$ , so that nodes that are better separated from already selected nodes, but also those that are closer to  $\zeta$  are preferred.

To control separation, we choose a *standard distance*  $\rho_\zeta$  defined as

$$\rho_\zeta := \frac{\delta}{6} \sum_{i=1}^6 \|\zeta - \xi_i\|,$$

where  $\xi_1, \dots, \xi_6$  are the six closest to  $\zeta$  nodes in  $\Xi \setminus \{\zeta\}$ ,  $\|\cdot\|$  denotes the Euclidean norm in  $\mathbb{R}^3$ , and  $\delta$  is a user-defined parameter satisfying  $0 < \delta < 1$ .

Recall that an *octant* centered at the origin in 3D is a cone that consists of points  $(x_1, x_2, x_3) \in \mathbb{R}^3$  such that  $\epsilon_i x_i \geq 0$ ,  $i = 1, 2, 3$ , where  $\epsilon_i \in \{-1, 1\}$ . The octants are not disjoint, therefore we reduce the boundary of some octants to make sure that for each point with e.g.  $x_1 = 0$  there is only one octant that contains it, see [7]. The points in a neighborhood of  $\zeta$  are classified according to 8 octants centered at  $\zeta$ . In [7, Algorithm 2] we split each octant in two *half-octants*, leading to the partition of the space around  $\zeta$  in 16 cones, and in this paper we also consider *one-third-octants* defined by the condition  $\max\{|x_1|, |x_2|, |x_3|\} = |x_i|$ ,  $i = 1, 2, 3$ , with appropriate reduction of the boundaries of some of them, which partitions the space into 24 disjoint cones.

We now describe the new selection algorithm that will be referred to as `oct-dist` in the rest of the paper.

**Algorithm 1** (`oct-dist`). *Input:*  $\Xi$  and  $\zeta \in \Xi_{\text{int}}$ . *Output:*  $\Xi_\zeta$ .

*Parameters:*

- $m$ : the number of nodes in the initial local cloud including  $\zeta$ ;
- $k$ : the target number of nodes in  $\Xi_\zeta$ ;
- $s \in \{1, 2, 3\}$ : the number of subdivisions of octants;
- $n$ : the number of candidate nodes in each octant,  $n = s\nu$  for some  $\nu \in \mathbb{N}$ ;
- $0 < \delta < 1$ : the standard distance tolerance.

I. Choose a set  $\Xi_{\text{cand}} \subset \Xi \setminus \{\zeta\}$  of candidate neighbors.

1. Choose the initial cloud  $\Xi_{\text{Init}} := \{\xi_1, \xi_2, \dots, \xi_{m-1}\} \subset \Xi \setminus \{\zeta\}$  consisting of  $m - 1$  nodes closest to  $\zeta$ , sorted by increasing distance to  $\zeta$ .
2. Compute  $\rho_\zeta := \frac{\delta}{6} \sum_{i=1}^6 \|\zeta - \xi_i\|$ .
3. Determine  $8s$  sets  $\tilde{\Omega}_j$ ,  $j = 1, 2, \dots, 8s$ , corresponding to the octants, for  $s = 1$ , half-octants for  $s = 2$ , or one-third-octants for  $s = 3$ , by collecting in each  $\tilde{\Omega}_j$  at most  $\nu$  nodes in  $\Xi_{\text{Init}}$  closest to  $\zeta$  and lying in the corresponding octant, half-octant or one-third-octant. We set  $\Xi_{\text{cand}} := \bigcup_{j=1}^{8s} \tilde{\Omega}_j$ .

4. Determine subsets  $O_j = \{\xi_1^j, \xi_2^j, \dots\}$ ,  $j = 1, 2, \dots, 8$ , of  $\Xi_{\text{cand}}$  consisting of the nodes lying in the eight octants as follows. If  $s = 1$ , then  $O_j = \tilde{O}_j$ ; otherwise  $O_j$  is the union of  $s$  sets of the type  $\tilde{O}_i$ . Assume that the numbering of the nodes is such that  $\|\zeta - \xi_1^j\| \leq \|\zeta - \xi_2^j\| \leq \dots \leq \|\zeta - \xi_{n_j}^j\|$ , with  $0 \leq n_j \leq n$ . Note that some  $O_j$  may be empty.
5. If  $\#\Xi_{\text{cand}} \leq k - 1$ , then STOP and return  $\Xi_\zeta := \Xi_{\text{cand}} \cup \{\zeta\}$ .

II. Choose the influence set  $\Xi_\zeta \subset \Xi_{\text{cand}} \cup \{\zeta\}$ .

*Initialization:*  $\Xi_\zeta := \emptyset$ .

1. For  $j = 1$  to 8:  
If  $O_j \neq \emptyset$ , then  $\Xi_\zeta := \Xi_\zeta \cup \{\xi_1^j\}$ .
2. Set  $\Xi_{\text{cand}} := \Xi_{\text{cand}} \setminus \Xi_\zeta$ , such that  $\Xi_{\text{cand}} = \{\bar{\xi}_1, \bar{\xi}_2, \dots\}$ , where  $\bar{\xi}_1, \bar{\xi}_2, \dots$  are sorted by increasing distance to  $\zeta$ .
3. For  $i = 1$  to  $\#\Xi_{\text{cand}}$ :  
If  $\text{dist}(\bar{\xi}_i, \Xi_\zeta) \geq \rho_\zeta$ , then:
  - a.  $\Xi_\zeta := \Xi_\zeta \cup \{\bar{\xi}_i\}$ .
  - b. If  $\#\Xi_\zeta = k - 1$ , then STOP and return  $\Xi_\zeta := \Xi_\zeta \cup \{\zeta\}$ .
4. Set  $\rho_\zeta := \delta \rho_\zeta$  and GOTO II.2.

### Remarks

1. Based on our numerical experiments,  $m = 100$  seems a good choice for this parameter;  $s = 1$  with  $n = 3$  works well in most cases, but for less regularly distributed nodes larger values for  $s$  and  $n$  are sometimes advantageous. We suggest  $k = 17$  as default value, with smaller  $k$  sometimes giving better results on more regular nodes. We choose  $\delta$  between 0.7 and 0.9, with a higher value for more complicated 3D shapes, see more details in Section 5.
2. In the first stage of the algorithm the initial cloud of  $m - 1$  nearest neighbors of  $\zeta$  is reduced to the set  $\Xi_{\text{cand}}$  of at most  $8n$  nearby nodes that represent the directions of all octants from  $\zeta$ . Using a larger parameter  $s$  makes these candidate neighbors more evenly distributed at the expense of potentially larger distances to  $\zeta$ . If  $\Xi_{\text{cand}}$  contains less than  $k$  nodes, then we skip the second stage and return  $\Xi_\zeta := \Xi_{\text{cand}} \cup \{\zeta\}$ . Note that we usually choose  $n \geq k/8$ , so that this situation may only occur if some octants contain too few nodes of  $\Xi$  in the vicinity of  $\zeta$ .
3. In the second stage at most  $k - 1$  candidate nodes of  $\Xi_{\text{cand}}$  are selected into the set of influence  $\Xi_\zeta$ . First, the closest node in each octant is selected and removed from  $\Xi_{\text{cand}}$ . In Step II.3 we go over the remaining candidate nodes according to their distance to  $\zeta$ , and add them to  $\Xi_\zeta$  if they are separated from already selected nodes by at least the standard distance  $\rho_\zeta$ . This loop is terminated if  $k - 1$  candidate notes are selected, in which case we add  $\zeta$  itself to  $\Xi_\zeta$  and return this set. Otherwise, we relax the separation restriction by setting  $\rho_\zeta := \delta \rho_\zeta$ , and repeat the selection loop of Step II.3 with the remaining candidate nodes. This process will eventually terminate at Step II.3.b because the number of candidate nodes at the second stage is at least  $k$ , and the distance condition gradually weakens.

4. In the earlier versions of octant based selection [7, Algorithms 1 and 2], we modified the sets  $\Xi_\zeta$  in the following way when  $\Omega$  is not convex: For each ‘invisible’  $\xi \in \Xi_\zeta \setminus \{\zeta\}$  such that the segment  $(\zeta, \xi)$  intersects the boundary  $\partial\Omega$  of  $\Omega$ , we replaced  $\xi$  by the point  $\xi' \in (\zeta, \xi) \cap \partial\Omega$  closest to  $\zeta$ . We do not apply this step here because the new points  $\xi'$  tend to significantly reduce the separation distance of the nodes in  $\Xi_\zeta$  and often lead to stencils of poor quality. Clearly, using nodes  $\xi$  with  $(\zeta, \xi) \cap \partial\Omega \neq \emptyset$  may be harmful on domains that possess thin holes or cracks, with big jumps in the solution across them. A special treatment may be needed in this case, for example the initial cloud  $\Xi_{\text{Init}}$  at Step I.1 may be chosen in such a way that it does contain those neighbors  $\xi$  for which  $\zeta$  and  $\xi$  are not connected by a short path within  $\Omega$ . However, ‘invisible’ nodes do not normally seem to be a problem if the discretization set  $\Xi$  is sufficiently dense in  $\Omega$ .

### 3 RBF-FD weights

Once a set of influence  $\Xi_\zeta$  is selected, the weights  $w_{\zeta, \xi}$  of the numerical differentiation formula (2) can be computed by the radial basis function method (RBF-FD).

Let  $\Phi : \mathbb{R}^3 \rightarrow \mathbb{R}$  be a positive definite or conditionally positive definite radial basis function,  $\Phi(x) = \varphi(\|x\|)$ ,  $x \in \mathbb{R}^3$ , with continuous  $\varphi : \mathbb{R}_+ \rightarrow \mathbb{R}$ , see [2, 12, 23] for further details on these functions.

For each  $\zeta \in \Xi_{\text{int}}$ , the weights  $w_{\zeta, \xi}$  are determined by the exactness condition

$$\Delta s(\zeta) = \sum_{\xi \in \Xi_\zeta} w_{\zeta, \xi} s(\xi), \quad (4)$$

required for all functions of the form

$$s(x) = \sum_{\xi \in \Xi_\zeta} a_\xi \Phi(x - \xi) + \sum_{j=1}^L c_j p_j(x), \quad a_\xi, c_j \in \mathbb{R},$$

satisfying the side condition

$$\sum_{\xi \in \Xi_\zeta} a_\xi p_i(\xi) = 0, \quad i = 1, \dots, L,$$

where  $\{p_1, \dots, p_L\}$ ,  $L = \binom{\ell+2}{3}$ , is a basis for the linear space of trivariate polynomials of order at most  $\ell$  (that is, total degree at most  $\ell - 1$ ). As shown in [5], the RBF-FD weights  $w_{\zeta, \xi}$  are uniquely determined by these conditions as soon as  $\Phi$  is positive definite or conditionally positive definite of order at most  $\ell$ , and there is any solution  $\{v_{\zeta, \xi} : \xi \in \Xi_\zeta\}$  for the polynomial exactness condition

$$\Delta p_i(\zeta) = \sum_{\xi \in \Xi_\zeta} v_{\zeta, \xi} p_i(\xi), \quad i = 1, \dots, L. \quad (5)$$

We refer to [5] for a discussion of computational methods for  $w_{\zeta, \xi}$ .

As demonstrated in [1], particularly good results are obtained with polyharmonic RBF defined by  $\varphi(r) = r^\alpha$  with a polynomial term. In this paper we are interested in methods with expected convergence order  $\mathcal{O}(h^2)$ , and therefore use  $\varphi(r) = r^5$  with quadratic polynomial term ( $\ell = 3$ ), which seem the most appropriate setting for this goal.

## 4 Other stencil selection methods

In addition to Algorithm 1 (`oct-dist`), we consider for comparison several other stencil selection methods that produce influence sets of size not exceeding 20. This number is motivated by the recommendation of [1] that the number of nodes in  $\Xi_\zeta$  should be at least the double of the polynomial dimension  $L$ , which is 10 in our experiments with the polyhamonic RBF  $\varphi(r) = r^5$  and  $\ell = 3$ .

**tet** In this case a conforming triangulation  $\Delta$  of  $\Omega$  into tetrahedra with vertices at all nodes of  $\Xi$  is required, and  $\Xi_\zeta$  consists of  $\zeta$  and all nodes connected to it by an edge of  $\Delta$ . This leads to a system matrix with sparsity pattern identical with that of the finite element method with linear shape functions on the same triangulation. Note that although this approach does not seem particularly useful in the meshless context as it relies on a tetrahedral mesh, it is possible to obtain similar  $\Xi_\zeta$  by a local Delaunay triangulation in the neighborhood of  $\zeta$ , which may circumvent the main hurdles of mesh generation. This method produces sets of influence containing on average about 16 nodes in our experiments.

**oct** Stencil selection according to [7, Algorithm 2], where 100 nearest neighbors of  $\zeta$  are sorted into 16 cones obtained by bisecting eight coordinate octants, and, in addition to  $\zeta$ , the closest node in each half-octant is taken into  $\Xi_\zeta$ . Clearly, the number of nodes in  $\Xi_\zeta$  is at most 17.

**20near** The set of influence  $\Xi_\zeta$  consists of 20 nearest neighbors of  $\zeta$ , including  $\zeta$  itself. This is the cheapest and most commonly used method. As shown in [7] smaller number of neighbors leads to significantly larger errors. Occasionally we check the performance of the methods **30near** and **40near** that select 30, respectively 40, nearest neighbors of  $\zeta$ .

**pQR4sel** Starting with 100 nearest neighbors of  $\zeta$ , we select  $\Xi_\zeta$  by the pQR method of order 4, as described in [4, 8]. This results in at most 20 nodes unless the polynomial exactness condition (5) of order 4 cannot be satisfied on 100 neighbors, in which case the method fails.

The above methods are applied only for selecting the sets of influence, while the weights  $w_{\zeta,\xi}$  of (3) are obtained by the RBF-FD method described in Section 3, with  $\varphi(r) = r^5$  and  $\ell = 3$ . On the other hand, pQR selection method introduced in [4] already generates weights satisfying the polynomial exactness condition (5), and corresponding meshless finite difference method performs well in the numerical experiments presented in [8]. Moreover, since the number of selected nodes in this case does not exceed the polynomial dimension  $L$ , RBF-FD weights computed with the polynomial term of order  $\ell$  are only rarely different from the pQR weights of the same order. Hence, unless we choose a smaller order for RBF-FD, as in **pQR4sel**, there is no point in replacing pQR weights by almost always identical RBF-FD weights. Because of this we also consider the following two selection methods with pQR weights whose computation does not rely on radial basis functions.

**pQR3, pQR4** Starting with 100 nearest neighbors of  $\zeta$ , we select  $\Xi_\zeta$  by the pQR method [4, 8] of order 3 or 4. Note that even if pQR4 enforces exactness of the numerical differentiation weights for polynomials of order  $\ell = 4$  rather than 3, this does not

seem to lead to a higher order method, as seen in numerical experiments below and in [8]. The number of nodes in  $\Xi_\zeta$  is at most 10 for pQR3 and at most 20 for pQR4.

## 5 Numerical Experiments

In this section we present a number of numerical tests to compare the performance of the improved octant-based selection method `oct-dist` of Algorithm 1 with other selection approaches for the meshless finite difference method, and with the finite element method. We use MATLAB 2017b in all experiments. In particular, finite element solutions are computed by PDE Toolbox [20].

We check the performance of mFD methods on several different types of discretization nodes  $\Xi$ , produced either as the vertices of 3D triangulations, or as Cartesian grids or Halton quasi-random points inside  $\Omega$  combined with some discretization of the boundary.

In particular, for all test problems we run all methods on sets  $\Xi$  obtained as nodes of *optimized triangulations* produced by the command `generateMesh` of MATLAB PDE Toolbox, with target maximum edge size  $H_{\max} = H_0 2^{-i/3}$ ,  $i = 0, 1, \dots$ , where  $H_0$  is chosen individually for each test problems because of the differences in the size and complexity of the domains. The factor  $2^{-1/3}$  is chosen such that the number of interior vertices approximately doubles for the next value of  $H_{\max}$ , possibly after some warm-up on coarse triangulations. The other parameters of `generateMesh` are always set to  $H_{\min} = H_{\max}/3$  and  $H_{\text{grad}}=1.5$ . We set `GeometricOrder` to 1 for the computation of the first order finite element solution `fem1` based on linear shape functions and all versions of the meshless finite difference method. It is set to 2 when we compute the second order finite element solution `fem2` that employs quadratic shape function.

In addition, for each test problem we also generate  $\Xi_{\text{int}}$  as uniform Cartesian *grids* in the interior of  $\Omega$  with target spacing  $h = 0.9 H_{\max}$  and distance from the boundary at least  $0.25h$ . Similarly, as another option, the nodes  $\Xi_{\text{int}}$  with the same target average spacing  $h$  are generated from the 3D *Halton* quasi-random stream with the help of MATLAB command `qrandstream`, scaled to a cube containing  $\Omega$ , and cleared of points outside of  $\Omega$  and those at a distance less than  $0.25h$  from the boundary. In this cases we produce boundary nodes either by *orthogonal projection* to the boundary of interior nodes at distance less than  $h$ , or by using boundary nodes of the above optimized triangulation. Note that orthogonal projection was successfully applied for boundary and interface discretization in numerical experiments for elliptic interface problems in [8], even for higher order mFD methods with pQR selection. When  $\Omega$  is convex (Test Problem 1) we use projected boundary nodes and also test the first order finite element method `fem1` on the same set  $\Xi$ . A mesh required for this method is a 3D Delaunay triangulation of the nodes in  $\Xi$  produced by MATLAB's command `delaunayTriangulation`. This provides us with an opportunity to see how various methods perform on vertices of an *unoptimized triangulation*.

For non-convex domains `delaunayTriangulation` does not generate a triangulation of  $\Omega$ . In order to obtain unoptimized triangulations for such domains (Test Problems 2–4), we use Gmsh [15], where we switch off mesh smoothing and optimization by setting the parameters `-smooth` and `Mesh.Optimize` to zero. Similar to MATLAB mesh generation, we produce a sequence of meshes by setting the maximum characteristic length parameter to  $cl_{\max} = H_0 2^{-i/3}$ ,  $i = 0, 1, \dots$ , with individual  $H_0$  reported below for each test problem.

Once a numerical solution  $\hat{u} = [\hat{u}_\xi]_{\xi \in \Xi}$  is computed by either meshless finite difference

method (3), or by the finite element method, we measure the accuracy of this solution by the relative root mean square (RRMS) error on the interior nodes, given by

$$E_{\text{ref}} = \text{RRMS}(\hat{u}^{\text{ref}}, \hat{u}, \Xi_{\text{int}}) := \frac{\left( \sum_{\zeta \in \Xi_{\text{int}}} (\hat{u}_{\zeta}^{\text{ref}} - \hat{u}_{\zeta})^2 \right)^{1/2}}{\left( \sum_{\zeta \in \Xi_{\text{int}}} (\hat{u}_{\zeta}^{\text{ref}})^2 \right)^{1/2}}. \quad (6)$$

where the vector  $\hat{u}^{\text{ref}} = [\hat{u}_{\zeta}^{\text{ref}}]_{\zeta \in \Xi}$  represents a reference solution, obtained by either evaluating on  $\Xi_{\text{int}}$  the exact solution  $u$  of (1),  $\hat{u}_{\zeta}^{\text{ref}} := u(\zeta)$ ,  $\zeta \in \Xi$ , if it is known analytically, or by interpolating to  $\Xi_{\text{int}}$  a numerical solution from a much finer set of nodes. For this we employ MATLAB's command `scatteredInterpolant` with default settings, which makes use of piecewise linear interpolation over a triangulation of the nodes. Note that we write  $E_{\text{ref}} = \text{NaN}$  in the tables below when the weights of Section 3 cannot be found for some  $\zeta \in \Xi_{\text{int}}$ , which only happens when there are no weights satisfying the polynomial exactness condition (5). On rare occasions we write  $E_{\text{ref}} = \text{Inf}$ , which means that MATLAB failed to solve the system (3) because its matrix was singular to working precision.

In addition to the errors, we provide information about the density of the system matrices since various selection methods lead to sets of influence of different sizes. The density of a matrix  $A \in \mathbb{R}^{n \times n}$  is the average number of nonzero entries per row, computed as

$$\text{density} = \text{nnz}(A)/n, \quad (7)$$

where  $\text{nnz}(A)$  is the total number of nonzero entries in  $A$ . Note that we measure the density of the matrix of (3) and that of the finite element stiffness matrix after eliminating the Dirichlet boundary conditions. Therefore the density is lower for coarse discretization where a more significant percentage of the nodes is located on the boundary.

**Test Problem 1.** *Poisson equation  $\Delta u = 3e^{x+y+z}$  in the unit ball  $\Omega = \{(x, y, z) \in \mathbb{R}^3 : x^2 + y^2 + z^2 < 1\}$  with Dirichlet boundary conditions chosen such that the exact solution is  $u(x, y, z) = e^{x+y+z}$ .*

In the first experiment we obtain  $\Xi$  as vertices of the optimized triangulations produced by `generateMesh` as described above, with  $H_0 = 0.25$ . The results are presented in Table 1. The column marked `fem1` shows the error  $E_{\text{ref}}$  for the first order finite element method, whereas the other columns correspond to the meshless finite difference method with various versions of selection algorithms, as described in Sections 2 and 4. We reserved two columns for Algorithm 1, `oct-dist13` and `oct-dist17`, depending on the value of the parameter  $k = 13$  or  $17$ . Other parameters of Algorithm 1 are the same in both cases:  $s = 1$ ,  $n = 3$ ,  $\delta = 0.9$ . The last row of the table gives the density of the system matrix on the finest set of nodes.

In addition, Table 2 presents the errors and density for the second order finite element method on the nodes of the optimized triangulations obtained with  $H_0 = 0.5$  and `GeometricOrder = 2`.

The errors for all versions of the meshless finite difference method, including `tet` selection whenever this method does not fail, are smaller (sometimes more than 6 times smaller) than those of the finite element method `fem1` on the same nodes.

The errors of `fem2` in Table 2 on comparable sizes of  $\Xi_{\text{int}}$  are significantly better than for any method of Table 1. This is explained by the fact that the solution  $u$  is

# $\Xi_{\text{int}}$	FEM	Polyharmonic $r^5$ with quadratic polynomial						Pivoted QR	
		fem1	tet	oct	oct-dist13	oct-dist17	20near	pQR4sel	pQR3
245	5.4e-03	2.6e-03	2.9e-03	2.6e-03	2.7e-03	2.8e-03	3.1e-03	3.2e-03	2.9e-03
567	3.3e-03	NaN	2.1e-03	1.6e-03	1.8e-03	1.7e-03	1.3e-03	1.9e-03	1.7e-03
1142	1.8e-03	8.7e-04	5.8e-04	9.5e-04	8.0e-04	1.0e-03	6.3e-04	9.4e-04	1.0e-03
2523	1.0e-03	5.3e-04	4.2e-04	6.6e-04	5.5e-04	5.7e-04	3.5e-04	7.8e-04	5.9e-04
5207	5.9e-04	3.1e-04	2.6e-04	4.0e-04	2.9e-04	3.1e-04	2.1e-04	3.2e-04	3.5e-04
10780	3.8e-04	1.8e-04	1.5e-04	1.8e-04	9.7e-05	1.4e-04	1.0e-04	2.1e-04	2.2e-04
21730	2.3e-04	NaN	8.8e-05	1.2e-04	6.8e-05	9.0e-05	5.9e-05	1.1e-04	1.4e-04
43956	1.4e-04	NaN	4.5e-05	7.2e-05	3.6e-05	4.1e-05	2.7e-05	8.1e-05	8.5e-05
88936	8.9e-05	NaN	3.0e-05	4.4e-05	2.2e-05	2.7e-05	1.3e-05	5.4e-05	5.3e-05
density:	14.6	14.6	16.5	12.7	16.5	19.4	19.4	9.8	19.4

Table 1: Test Problem 1: RRMS errors  $E_{\text{ref}}$  on interior nodes of the optimized triangulations with  $H_0 = 0.25$ . The last row shows the density of the system matrix on the finest set of nodes.

# $\Xi_{\text{int}}$	272	824	1113	2357	5127	10138	21821	44238	90396	density
fem2	9.4e-04	3.8e-04	2.8e-04	1.2e-04	6.1e-05	2.8e-05	1.3e-05	5.8e-06	3.0e-06	27.3

Table 2: Test Problem 1: RRMS error  $E_{\text{ref}}$  of the quadratic finite element method for the optimized triangulations with  $H_0 = 0.5$ . The last column shows system matrix density on the finest set of nodes.

a very smooth, infinitely differentiable function, so that higher order methods such as `fem2` should be beneficial. However, we also notice that the density 27.3 of the system matrix of `fem2` is significantly higher than the densities seen in Table 1.

We notice that smaller errors in Table 1 clearly correlate with higher density. Comparing methods of the same density, we see that `oct-dist17` significantly outperforms `oct`, and `pQR4sel` outperforms `20near` and `pQR4`. In order to take into account the differences in density, we compare in Figure 1(a) the errors of different methods as functions of the nominal number of nonzeros (nominal `nnz`) of the system matrix, computed as the number of interior nodes  $\#\Xi_{\text{int}}$  multiplied by the density on the finest set of nodes (provided in the tables). Note that the number of nonzeros in the system matrix determines the cost of matrix-vector multiplication, and therefore the cost per iteration when solving the system by iterative methods. Figure 1(a) does not include `tet` because it fails on several sets  $\Xi$ , and for `oct-dist` we included the better performing version with  $k = 17$  and left out the one with  $k = 13$ .

We see that the best performing selection methods for the nodes of the optimized triangulation are `oct-dist` with  $k = 17$  and `pQR4sel`. In particular, both of them produce significantly more accurate solutions than `fem1`.

In the next experiment we generate  $\Xi$  as a uniform grid in the interior of  $\Omega$ , with boundary nodes produced by orthogonal projection as explained in the beginning of this section. The results are presented in Table 3 and Figure 1(b). For the meshless finite difference method we take advantage of the grid structure of the nodes, and use for the Laplacian in (2) the classical 7-node stencil,

$$\begin{aligned} \Xi_{\zeta}^{7\text{star}} &= \{\zeta, \zeta \pm (h, 0, 0), \zeta \pm (0, h, 0), \zeta \pm (0, 0, h)\}, \\ w_{\zeta, \zeta} &= -6h^{-2}, \quad w_{\zeta, \xi} = h^{-2}, \quad \xi \in \Xi_{\zeta} \setminus \{\zeta\}, \end{aligned} \tag{8}$$

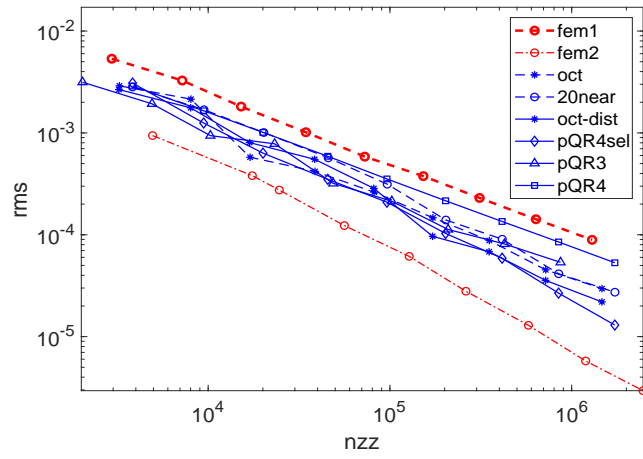
whenever possible. These weights are exact for polynomials of order 4. The same weights

are also obtained by the radial basis exactness condition (4) on  $\Xi_\zeta^{7\text{star}}$  when  $\ell = 3$  or 4. Thus, specific stencil selection and weight computation methods described in Sections 2–4 are only applied for  $\zeta \in \Xi_{\text{int}}$  near the boundary such that  $\Xi_\zeta^{7\text{star}} \not\subset \Xi_{\text{int}}$ . Therefore the density of the system matrix on finer discretizations only slightly exceeds 7. The results for the finite element method `fem1` are obtained on a 3D Delaunay triangulation of the nodes in  $\Xi$  created by MATLAB command `delaunayTriangulation`, which produces a triangulation of  $\Omega$  since this domain (the unit ball) is convex. We use  $k = 18$  for `oct-dist`, with values of other parameters of this method the same as above. The errors demonstrated by all versions of the mFD method, except of `tet` that again fails on several sets of nodes, are very close to each other and significantly better than the errors of the finite element method, especially if the density of the system matrices is taken into account. In Table 3 we also included selection of 30 nearest nodes (`30near`), which does not increase the density of the system matrix essentially because of the 7-node stencils still used in most places. The errors are slightly better than those for `20near`. Therefore larger sets of influence may be recommended in this case. However, this improvement may be attributed to the high smoothness of  $u$  as it does not happen for more interesting problems considered below, as will be demonstrated for Test Problem 2. Comparison of Figures 1(a) and 1(b) shows that the error to `nnz` ratio is better for mFD methods on interior grid nodes than for those on the optimized triangulation, whereas `fem1` shows the opposite behavior.

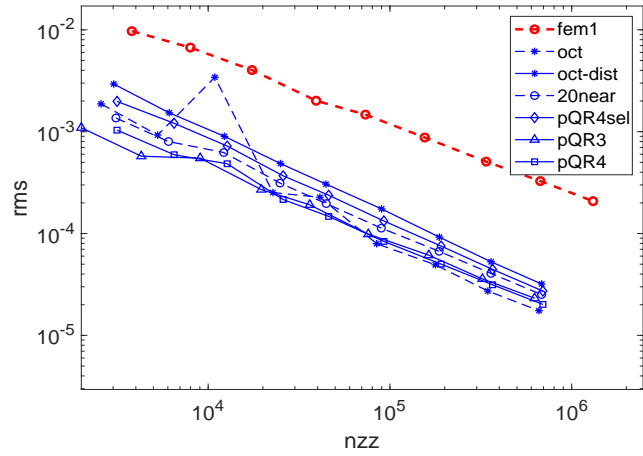
# $\Xi_{\text{int}}$	FEM	Polyharmonic $r^5$ with quadratic polynomial						Pivoted QR	
		fem1	tet	oct	oct-dist	20near	30near	pQR4sel	pQR3
304	9.7e-03	9.9e-04	1.9e-03	2.9e-03	1.4e-03	6.6e-04	2.0e-03	1.1e-03	1.0e-03
624	6.7e-03	6.4e-04	9.3e-04	1.5e-03	8.0e-04	4.1e-04	1.2e-03	5.7e-04	5.9e-04
1308	4.0e-03	3.5e-04	3.4e-03	9.0e-04	6.2e-04	3.9e-04	7.2e-04	5.5e-04	4.8e-04
2822	2.0e-03	2.1e-04	2.5e-04	4.9e-04	3.1e-04	2.0e-04	3.7e-04	2.7e-04	2.2e-04
5196	1.5e-03	1.4e-04	2.3e-04	3.1e-04	2.0e-04	1.3e-04	2.4e-04	1.9e-04	1.5e-04
10935	8.8e-04	NaN	7.9e-05	1.7e-04	1.1e-04	8.3e-05	1.3e-04	9.9e-05	8.4e-05
23436	5.1e-04	4.9e-05	4.9e-05	9.2e-05	6.7e-05	5.0e-05	7.5e-05	6.1e-05	5.0e-05
46251	3.3e-04	NaN	2.7e-05	5.3e-05	4.1e-05	3.2e-05	4.5e-05	3.6e-05	3.1e-05
89372	2.1e-04	NaN	1.8e-05	3.2e-05	2.5e-05	2.0e-05	2.7e-05	2.3e-05	2.0e-05
density	14.7	7.4	7.4	7.7	7.6	8.3	7.8	7.0	7.8

Table 3: Test Problem 1: RRMS errors  $E_{\text{ref}}$  for uniform interior grids and projected boundary nodes. For meshless finite difference methods we use classical 7-node grid stencil whenever possible.

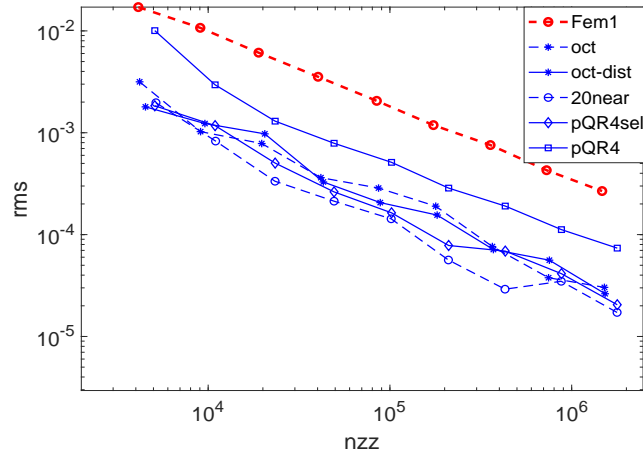
In the last experiment for Test Problem 1, we use Halton interior nodes, with boundary nodes obtained by orthogonal projection. The results can be found in Table 4 and Figure 1(c), where for `fem1` a 3D Delaunay triangulation of  $\Xi$  is again created by MATLAB command `delaunayTriangulation`. We use  $\delta = 0.9$ ,  $s = 1$ ,  $n = 3$  and  $k = 17$  for `oct-dist`. In this experiment selection methods `tet` and `pQR3` do not perform well, therefore we do not include them in Figure 1(c). The extremely large errors of `pQR3` for the two finest sets of nodes indicate instability of the system matrix, which will be investigated in detail for Test Problem 2. The method `pQR4` shows significantly higher errors than the remaining selection algorithms, including the simple selection of 20 nearest points `20near`, which even looks like the best option in this case. We notice that the mFD method performs very well on Halton nodes, sometimes even better than on the optimized triangulations, whereas the errors of `fem1` are the highest for this type of  $\Xi$ .



(a) Optimized triangulation



(b) Interior grid and projected boundary nodes



(c) Halton interior and projected boundary nodes

Figure 1: Test Problem 1: RRMS errors as functions of nominal  $\text{nnz}$ , corresponding to (a) Tables 1 and 2, where  $\text{oct-dist}$  stands for  $\text{oct-dist17}$ , (b) Table 3, (c) Table 4

# $\Xi_{\text{int}}$	FEM	Polyharmonic $r^5$ with quadratic polynomial					Pivoted QR	
		fem1	tet	oct	oct-dist	20near	pQR4sel	pQR3
303	1.7e-02	NaN	3.2e-03	1.8e-03	2.0e-03	1.8e-03	3.9e-03	1.0e-02
627	1.1e-02	NaN	1.0e-03	1.2e-03	8.3e-04	1.2e-03	1.6e-03	3.0e-03
1308	6.1e-03	NaN	7.8e-04	9.8e-04	3.3e-04	5.0e-04	9.4e-04	1.3e-03
2699	3.5e-03	NaN	3.6e-04	3.3e-04	2.1e-04	2.6e-04	3.8e-04	7.9e-04
5493	2.1e-03	NaN	2.9e-04	2.1e-04	1.4e-04	1.6e-04	2.1e-04	5.1e-04
11140	1.2e-03	NaN	1.9e-04	1.6e-04	5.6e-05	7.8e-05	1.5e-04	2.9e-04
22561	7.6e-04	NaN	7.6e-05	7.1e-05	2.9e-05	6.9e-05	1.2e-04	1.9e-04
45513	4.3e-04	NaN	3.8e-05	5.6e-05	3.5e-05	4.1e-05	3.0e+08	1.1e-04
91655	2.7e-04	NaN	3.0e-05	2.6e-05	1.7e-05	2.1e-05	2.1e+08	7.4e-05
density	16.0	16.0	16.5	16.7	19.4	19.4	9.8	19.4

Table 4: Test Problem 1: RRMS error  $E_{\text{ref}}$  for Halton quasi-random interior nodes and projected boundary nodes.

It is well known that the performance of the finite element method depends on the mesh quality, in particular the shape regularity of the elements, see e.g. [14]. We therefore provide in Table 5 information about the distribution of the aspect ratios of tetrahedra for each of the three types of triangulations in the above experiments. The (inverse) *aspect ratio* of a tetrahedron  $T$  is given by

$$\gamma_T = 2\sqrt{6} \rho_T / h_T \quad (9)$$

where  $h_T$  is the diameter and  $\rho_T$  is the inradius of the tetrahedron  $T$  [16, p. 1317]. The coefficient  $2\sqrt{6}$  is chosen such that  $0 \leq \gamma_T \leq 1$ , with  $\gamma_T = 0$  for a degenerate tetrahedron and  $\gamma_T = 1$  for a regular tetrahedron. The quality of  $T$  is higher when  $\gamma_T$  is larger. Table 5 shows the minimum and the average values of  $\gamma_T$  over all tetrahedra of the finest triangulation in each Table 1, 3 and 4, as well as percentages of tetrahedra with  $\gamma_T$  in the ranges 0–0.25, 0.25–0.5, 0.5–0.75 and 0.75–1.0. We compute these statistics using Gmsh [15] for the finest triangulation in each experiments. We see that the quality of the optimized triangulation used in the first experiment is significantly higher than that of the other two triangulations, which explains the smaller errors of `fem1` on the optimized triangulation. In contrast to this, higher shape regularity of the optimized triangulation does not seem to be advantageous for the mFD methods.

Triangulation	min $\gamma$	avg $\gamma$	$0 < \gamma \leq 0.25$	$0.25 < \gamma \leq 0.5$	$0.5 < \gamma \leq 0.75$	$0.75 < \gamma \leq 1.0$
Optimized	0.50	0.87	0.0%	0.0%	6.3%	93.7%
Delaunay/Grid	4.6e-02	0.68	0.1%	2.2%	96.5%	1.2%
Delaunay/Halton	1.8e-03	0.63	4.8%	21.0%	45.8%	28.4%

Table 5: Test Problem 1: Statistics of the aspect ratio  $\gamma_T$  for the simplices of three 3D triangulations used in the tests with finite element method `fem1`, namely optimized triangulation as in Table 1, Delaunay triangulation of gridded nodes as in Table 3, and Delaunay triangulation of Halton nodes as in Table 4.

**Test Problem 2 (BracketTwoHoles).** *Poisson equation  $\Delta u = -10$  with zero Dirichlet boundary conditions on the domain  $\Omega$  defined in the STL file ‘BracketTwoHoles.stl’ shipped with MATLAB PDE Toolbox [20], see Figure 2.*

Since the exact solution of this problem is not known, we compute a reference solution

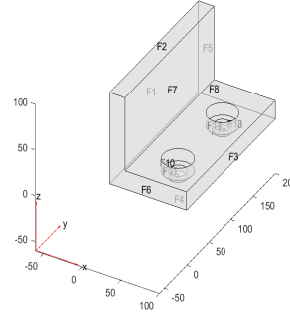


Figure 2: Test Problem 2: Domain `BracketTwoHoles`; the 3D plot is produced by MATLAB PDE Toolbox command `pdegplot`.

by the second order finite element method on a triangulation with 1605099 nodes obtained by `generateMesh` with  $H_{\max} = 1.7$ ,  $H_{\min} = H_{\max}/3$ ,  $H_{\text{grad}} = 1.5$  and `GeometricOrder = 2`.

Similar to Test Problem 1, for our first experiment we generate  $\Xi$  as vertices of optimized triangulations produced by `generateMesh`, with  $H_0 = 8.5$ . We use parameter values  $\delta = 0.9$ ,  $s = 1$ ,  $n = 3$  and  $k = 13$  for `oct-dist`. The results are presented in Table 6. The errors of the second order finite element method `fem2` for optimized triangulations with  $H_0 = 17$  are shown in Table 7. Figure 4(a) presents the same errors as functions of nominal `nnz`. We see here that the versions `oct-dist`, `pQR3` and `pQR4` of mFD produce more accurate solutions than `fem1` and compete with the second order method `fem2`.

# $\Xi_{\text{int}}$	FEM	Polyharmonic $r^5$ with quadratic polynomial					Pivoted QR	
		fem1	tet	oct	oct-dist	20near	pQR4sel	pQR3
871	5.5e-02	4.3e-02	6.1e-02	3.2e-02	7.6e-02	7.7e-02	3.8e-02	2.5e-02
2086	4.3e-02	NaN	5.6e-02	3.5e-02	6.3e-02	6.2e-02	3.2e-02	2.2e-02
4150	3.4e-02	2.9e-02	3.7e-02	2.4e-02	4.4e-02	4.5e-02	2.4e-02	1.6e-02
9628	1.9e-02	1.8e-02	2.4e-02	1.4e-02	3.3e-02	3.2e-02	1.2e-02	1.1e-02
19493	1.5e-02	1.3e-02	2.0e-02	1.2e-02	2.4e-02	2.2e-02	1.1e-02	9.5e-03
41215	8.6e-03	NaN	1.1e-02	6.2e-03	1.5e-02	1.5e-02	7.8e-03	5.2e-03
86699	6.8e-03	NaN	9.3e-03	6.0e-03	1.1e-02	1.1e-02	6.1e-03	4.4e-03
178432	4.5e-03	NaN	7.2e-03	4.7e-03	6.8e-03	7.5e-03	4.9e-03	3.1e-03
density	14.2	14.2	15.9	12.4	18.8	18.7	9.5	18.7

Table 6: Test Problem 2: RRMS errors  $E_{\text{ref}}$  for optimized triangulations with  $H_0 = 8.5$ .

# $\Xi_{\text{int}}$ :	1197	2647	4121	9507	21034	39659	87900	173262	density
fem2:	4.0e-02	2.3e-02	1.6e-02	9.7e-03	6.6e-03	5.0e-03	3.1e-03	2.3e-03	25.9

Table 7: Test Problem 2: RRMS errors  $E_{\text{ref}}$  of the quadratic finite element method for optimized triangulations with  $H_0 = 17$ .

In the next experiment we generate  $\Xi$  as vertices of an unoptimized triangulation of  $\Omega$ . Since this domain is not convex, `delaunayTriangulation` is not available to triangulate it, and we use Gmsh with smoothing and optimization switched off, as explained above, with  $H_0 = 8.5$ . The quality of both triangulations is compared in Table 8. Parameters

of `oct-dist` are chosen as  $\delta = 0.9$ ,  $s = 3$ ,  $n = 6$  and  $k = 17$ . The results are presented in Table 9 and Figure 4(b). The only selection methods included in Figure 4(b) are `oct-dist`, `pQR4` and `pQR4sel` because `tet`, `oct` and `20near` fail to generate sets of influence with weights satisfying the exactness condition (5), whereas `pQR3` too often produces high errors and even leads to a singular system matrix of (3) on the finest node set. Nevertheless, the error of `pQR3` for the discretization with  $\#\Xi_{\text{int}} = 86541$  is among the best, with by far lower density of the system matrix than in any other method in the table. In fact, the error is also poor for `pQR4` on one of the sets  $\Xi$ , see the peak in its plot in Figure 4(b), but we nevertheless included `pQR4` in the figure because its errors for the other node sets are the best compared to other methods.

Triangulation	min $\gamma$	avg $\gamma$	$0 < \gamma \leq 0.25$	$0.25 < \gamma \leq 0.5$	$0.5 < \gamma \leq 0.75$	$0.75 < \gamma \leq 1.0$
Optimized	0.51	0.88	0.0%	0.0%	2.8%	97.2%
Unoptimized	3.1e-05	0.78	1.7%	5.8%	25.1%	67.4%

Table 8: Test Problem 2: Statistics of the aspect ratio  $\gamma_T$  for the simplices of two types of 3D triangulations used in the tests with finite element method `fem1`, namely an optimized triangulation as in Table 6, and an unoptimized one as in Table 9.

# $\Xi_{\text{int}}$	FEM	Polyharmonic $r^5$ with quadratic polynomial							Pivoted QR	
		fem1	tet	oct	oct-dist	20near	30near	40near	pQR4sel	pQR3
726	1.3e-01	NaN	NaN	7.1e-02	NaN	NaN	NaN	1.1e-01	2.1e-01	1.1e-01
1491	1.1e-01	NaN	NaN	7.1e-02	NaN	NaN	1.2e-01	8.3e-02	1.8e+00	4.5e-02
2529	6.8e-02	NaN	NaN	4.9e-02	NaN	NaN	NaN	5.8e-02	1.2e-01	3.4e-02
4954	5.0e-02	NaN	NaN	3.6e-02	NaN	NaN	NaN	4.1e-02	3.6e-02	1.6e-01
9940	3.4e-02	NaN	NaN	2.6e-02	NaN	NaN	5.4e-02	3.2e-02	7.3e-02	1.5e-02
19834	2.4e-02	NaN	NaN	1.7e-02	NaN	NaN	NaN	2.2e-02	6.7e-02	1.3e-02
41941	1.6e-02	NaN	NaN	1.3e-02	NaN	NaN	3.0e-02	1.5e-02	9.9e-03	8.1e-03
86541	1.1e-02	NaN	1.0e-02	9.6e-03	NaN	NaN	2.1e-02	1.1e-02	6.7e-03	5.9e-03
178450	7.4e-03	NaN	NaN	6.7e-03	NaN	NaN	NaN	7.7e-03	Inf	3.9e-03
density	14.9	14.9	15.9	15.9	18.4	27.4	36.3	18.8	9.6	18.8

Table 9: Test Problem 2: RRMS errors  $E_{\text{ref}}$  for unoptimized triangulations.

Since the pQR method produces accurate numerical differentiation formulas [4], the reasons for the large errors seen on certain node sets seems to be related to the global properties of the linear system (3). In order to investigate this, we have computed the *stability constant*

$$\sigma := \text{condest}(A^T)/\|A\|_\infty, \quad (10)$$

where  $A$  is the system matrix of (3), see Table 10. This formula, suggested in [21], uses an efficient estimator of the 1-norm condition number available in MATLAB via command `condest`. Therefore  $\sigma$  is a good approximation of the norm  $\|A^{-1}\|_\infty$  that measures stability in the classical error analysis of the Finite Difference Method for elliptic problems. Unfortunately, there are no theoretical results that would allow to estimate the stability constant, and the error analysis of the meshless finite difference methods is underdeveloped [3]. Nevertheless, the numbers in Table 10 indicate that large errors are always associated with relatively high values of  $\sigma$ . For the two most stable methods `oct-dist` and `pQR4sel`, with monotone graphs in Figure 4(b), we always see  $\sigma < 100$ , whereas `pQR4` produces matrices with  $\sigma \geq 300$  for  $i \leq 5$ , and  $\sigma > 3000$  for the peak of Figure 4(b) at  $i = 3$ . The large errors of `pQR3` for  $i \leq 5$  and  $i = 8$  correspond

to extremely large  $\sigma$ , and very good results for  $i \in \{6, 7\}$  correspond to  $\sigma \approx 61$ , close to the minimum of  $\sigma = 58.6$  in Table 10. Note that  $56.3 \leq \sigma \leq 68.9$  in all mFD tests for optimized triangulations reported in Table 6.

# $\Xi_{\text{int}}$	oct-dist	pQR4sel	pQR3	pQR4
726	91.4	76.1	2.9e+16	1.6e+03
1491	58.6	82.9	1.6e+17	3.4e+03
2529	59.0	68.2	1.6e+17	5.9e+02
4954	58.7	64.9	2.1e+17	3.5e+03
9940	59.2	58.6	2.5e+16	7.0e+02
19834	59.8	59.6	6.6e+15	3.0e+02
41941	60.2	60.3	60.6	60.7
86541	60.6	60.5	60.8	60.7
178450	60.7	60.7	inf	61.1

Table 10: Test Problem 2: stability constant  $\sigma$  for unoptimized triangulations.

Since **20near** fails completely, we tried to increase the number of nearest neighbors, and included in Table 9 the errors for **30near** and **40near** even if the density of the system matrix gets much higher. We see that the results remain very poor even for 40 nearest neighbors. This may be related to the fact that STL models often include many thin and long triangles on the boundary, and typical triangulation algorithms start by discretizing boundary edges, then boundary triangles, and only after that proceed to adding vertices in the interior of the domain. As a result, neighborhoods of certain interior nodes include many coplanar boundary nodes that are not favorable for numerical differentiation, see Figure 3. Therefore it is helpful when the selection algorithm abandons some of these coplanar nodes even if they are the closest neighbors to  $\zeta$ .

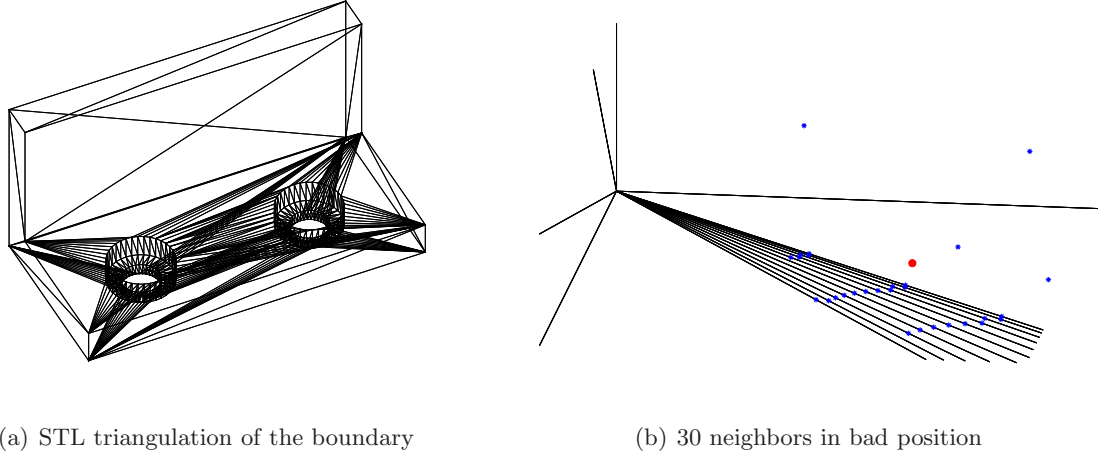


Figure 3: Test Problem 2: (a) STL model and (b) 30 nearest vertices of the unoptimized triangulation for the node marked as a red dot. Note that all nodes shown are lying in the horizontal plane except of the red node itself and the two topmost nodes.

In the next experiment we generate nodes by a uniform grid in the interior and orthogonal projection to the boundary, again using the classical 7-node grid stencil whenever

possible. Unfortunately, no selection method shows a good performance in this case. The methods `20near`, `oct` and `oct-dist` fail to provide polynomial exactness (5). The errors of `30near`, `pQR4sel`, `pQR3` and `pQR4` are shown in Table 11 and are disappointing. The data in Table 11 show that situations where the error of the mFD method is particularly bad correspond to stability constant several magnitudes higher than the ‘normal’ values of around 60.

# $\Xi_{\text{int}}$	30near		pQR4sel		pQR3		pQR4	
	$E_{\text{ref}}$	$\sigma$	$E_{\text{ref}}$	$\sigma$	$E_{\text{ref}}$	$\sigma$	$E_{\text{ref}}$	$\sigma$
1004	1.3e-01	67.4	1.2e-01	617.9	1.2e-01	884.1	3.1e-01	2.1e+04
2572	1.1e-01	68.0	6.0e-02	63.5	4.7e-02	62.1	2.0e+00	1.5e+04
4344	2.0e-01	2.1e+03	4.4e-01	9.0e+03	2.0e-01	4.1e+03	7.4e+00	2.6e+06
8883	4.6e-01	5.9e+03	5.1e-01	1.2e+04	5.9e-01	5.4e+03	9.4e+00	4.7e+05
21228	2.8e-02	62.9	1.6e-02	61.8	1.5e-02	362.4	4.8e-02	1.2e+03
45808	3.6e-02	64.0	1.7e-02	62.2	1.1e-02	61.7	2.6e-01	3.6e+03
92528	2.0e-02	62.9	1.7e-02	62.8	6.7e-03	61.9	3.4e-02	299.0
176179	6.8e-01	7.8e+03	7.8e-01	3.5e+04	7.3e-01	1.5e+04	8.1e+00	6.5e+06
density	10.5		7.1		6.9		7.1	

Table 11: Test Problem 2: RRMS error  $E_{\text{ref}}$  and stability constant  $\sigma$  for uniform interior grids and projected boundary nodes. The 7-node grid stencil (8) is used whenever possible.

The performance of mFD is much better if we combine interior grid nodes with the discretization of the boundary taken from the optimized triangulation of the first experiment for this test problem. More precisely, we choose  $H_0 = 8.5$  and generate, for each  $i = 0, \dots, 7$ , the interior nodes as a grid with target spacing  $h = 0.9 \text{Hmax}$ , where  $\text{Hmax} = H_0 2^{-i/3}$ . To obtain boundary nodes, we run `generateMesh` with the above  $\text{Hmax}$ , and use the boundary vertices of the resulting triangulation as boundary nodes of  $\Xi$ . The results are presented in Table 12 and Figure 4(c). Parameters of `oct-dist` are  $\delta = 0.9$ ,  $s = 1$ ,  $n = 3$  and  $k = 18$ , as in the case of interior grid nodes for Test Problem 1. The performance of mFD with all selection methods but `pQR4` is good, although the error graphs in Figure 4(c) are not monotone. In particular, the set  $\Xi$  with 45808 interior nodes ( $i = 5$ ) seems unfavorable for all methods. Nevertheless, looking for example at the graph for `pQR3`, we see that the point corresponding to  $i = 4$  that makes this graph looking so irregular, in fact shows exceptionally good error, by far the best for comparable number of interior nodes (around 20000) in all experiments for Test Problem 2. The stability constant  $\sigma$  in all tests in Table 12 except `pQR4` satisfies  $58.2 \leq \sigma \leq 67.4$ . For `pQR4` we have  $\sigma = 90.4$  when  $i = 2$  and 413.0 when  $i = 5$ , otherwise  $\sigma$  is also below 70, which fits well into the data in Table 12, where the errors for  $i = 2$  and 5 are significantly higher for `pQR4` than with other selection methods. In addition to `20near`, we included in Table 12 the errors of mFD for selection methods `30near` `40near`. However, in contrast to Test Problem 1, this does not improve the error in comparison to `20near`.

In the last experiment we generate interior nodes of  $\Xi$  from the Halton sequence of quasi-random numbers and the boundary nodes by the orthogonal projection. Surprisingly, the results are much better than in the case of interior grids combined with projected boundary nodes, see Table 13 and Figure 4(d). The parameters of `oct-dist` are the same as in the case of Halton interior nodes for Test Problem 1:  $\delta = 0.9$ ,  $s = 1$ ,  $n = 3$  and  $k = 17$ . We see that the best errors delivered by `oct-dist` and `pQR4sel` are not much higher than those achieved on the optimized triangulation. Selection meth-

# $\Xi_{\text{int}}$	Polyharmonic $r^5$ with quadratic polynomial						Pivoted QR	
	oct	oct-dist	20near	30near	40near	pQR4sel	pQR3	pQR4
1004	7.0e-02	5.4e-02	4.9e-02	6.7e-02	6.4e-02	3.8e-02	2.3e-02	7.0e-02
2572	5.5e-02	4.4e-02	4.2e-02	5.5e-02	4.9e-02	5.3e-02	3.9e-02	2.7e-01
4344	4.2e-02	3.7e-02	2.9e-02	3.8e-02	3.7e-02	2.8e-02	3.1e-02	3.7e-02
8883	2.9e-02	2.4e-02	1.7e-02	2.5e-02	3.0e-02	1.7e-02	2.3e-02	2.7e-02
21228	1.2e-02	1.2e-02	9.5e-03	1.2e-02	1.3e-02	8.7e-03	6.1e-03	2.0e-02
45808	1.7e-02	1.1e-02	1.1e-02	1.4e-02	1.2e-02	1.5e-02	1.1e-02	7.7e-02
92528	5.5e-03	3.9e-03	3.8e-03	4.8e-03	4.8e-03	5.2e-03	4.6e-03	1.8e-02
176179	8.1e-03	3.7e-03	4.0e-03	3.8e-03	1.2e-02	2.9e-03	4.8e-03	1.1e-02
density	7.9	8.2	8.6	9.9	11.4	8.6	7.0	8.6

Table 12: Test Problem 2: RRMS error  $E_{\text{ref}}$  for uniform interior grids and boundary nodes from optimized triangulations. The 7-node grid stencil (8) is used whenever possible.

ods **tet** and **oct** failed to provide influence sets satisfying (5). The errors of **pQR3** and **pQR4** are very high, therefore we did not include them in the figure. The irregularities of the plots in Figure 4(d) match well the behavior of the stability constant: we have  $\sigma = 546.9$  when  $i = 1$ , otherwise  $61.0 \leq \sigma \leq 80.1$  for **oct-dist**;  $\sigma = 138.5$  when  $i = 3$ , otherwise  $60.8 \leq \sigma \leq 63.0$  for **pQR4sel**, except the coarsest node set ( $i = 0$ ), where  $\sigma = 582.7$  somehow does not lead to an exceptionally high error. For **20near**,  $\sigma$  reduces from 1854.9 to 63.0 between  $i = 0$  and  $i = 4$ , rises to 118.4 for  $i = 6$ , and again falls to 62.9 for  $i = 7$ .

# $\Xi_{\text{int}}$	Polyharmonic			Pivoted QR	
	oct-dist	20near	pQR4sel	pQR3	pQR4
1165	6.9e-02	9.2e-02	1.0e-01	9.2e-01	3.3e+00
2474	2.7e-01	7.7e-02	6.4e-02	8.0e-02	3.7e-01
5187	2.7e-02	8.3e-02	5.2e-02	2.9e+00	8.1e-01
10754	1.9e-02	5.3e-02	5.0e-02	2.3e-02	2.5e-01
22093	1.3e-02	1.5e-02	1.5e-02	3.3e-02	3.6e-01
45172	7.6e-03	1.8e-02	8.1e-03	2.0e-02	2.8e-01
91893	6.0e-03	2.8e-02	6.5e-03	1.6e-02	3.7e-02
186274	4.0e-03	9.0e-03	4.2e-03	5.1e-02	5.5e-02
density	16.3	18.8	18.9	9.6	18.9

Table 13: Test Problem 2: RRMS error  $E_{\text{ref}}$  for Halton interior nodes and projected boundary nodes.

**Test Problem 3 (ForearmLink).** Poisson equation  $\Delta u = -10$  with zero Dirichlet boundary conditions on the domain  $\Omega$  defined in the STL file ‘ForearmLink.stl’ shipped with MATLAB PDE Toolbox [20], see Figure 5.

A reference solution is computed by the second order finite element method on a triangulation with 641825 nodes obtained by `generateMesh` with  $\text{Hmax} = 6.8/2^{7/3} \approx 1.35$ ,  $\text{Hmin} = \text{Hmax}/3$ ,  $\text{Hgrad}=1.5$  and `GeometricOrder=2`.

Similar to the previous test problems, we run several numerical experiments using nodes of different types: vertices of optimized/unoptimized triangulations, interior Cartesian grids combined with boundary vertices of the optimized triangulation, and Halton interior nodes with projected nodes on the boundary. The results are presented in Tables 14–19 and Figure 6. For **oct-dist** we use  $\delta = 0.7$ , with other parameters  $s, n, k$

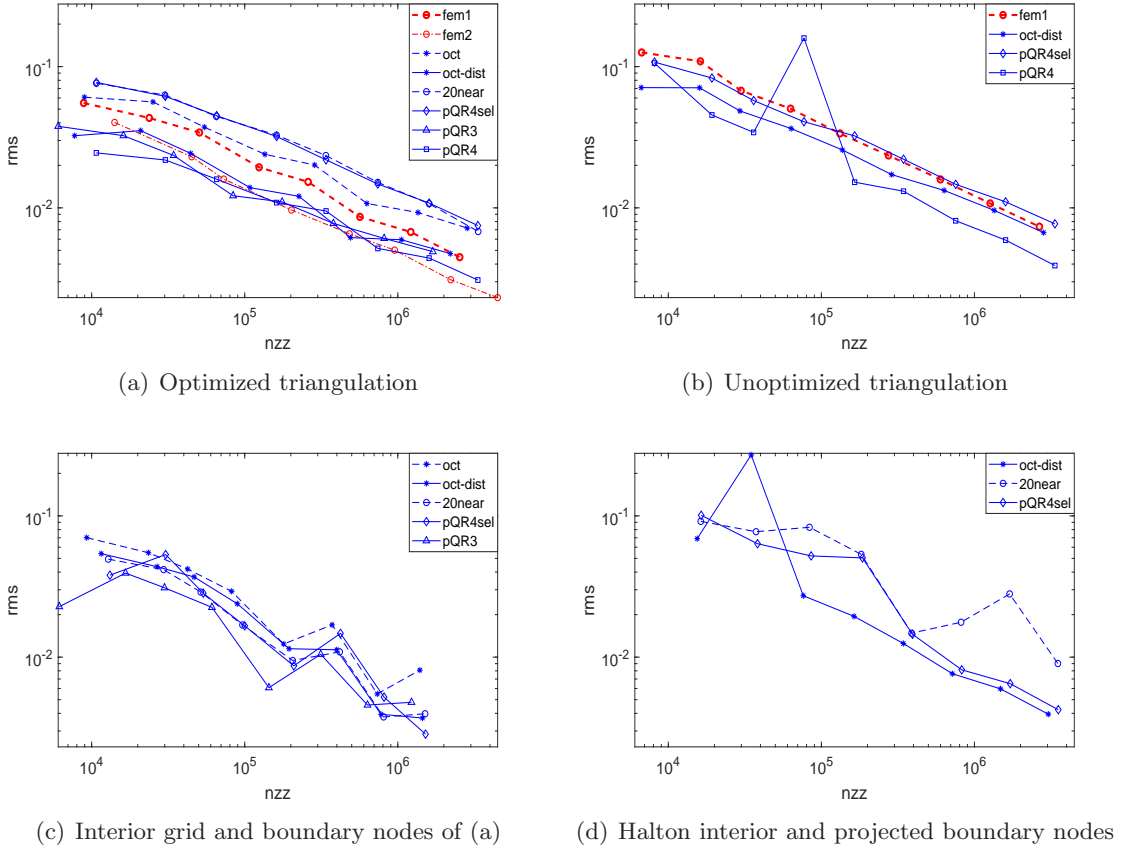


Figure 4: Test Problem 2: RRMS errors as functions of nominal  $\text{nnz}$ , corresponding to (a) Tables 6 and 7, (b) Table 9, (c) Table 12, (d) Table 13

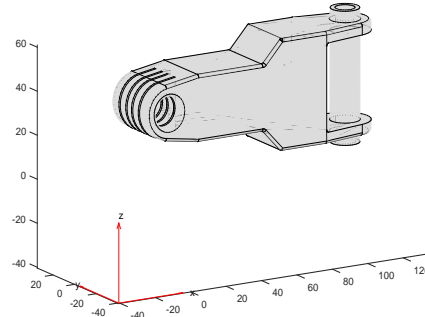


Figure 5: Test Problem 3: Domain `ForearmLink`.

reported in the captions of respective tables. Note that we omitted the high error of  $\text{pQR4sel}$  for  $i = 4$  in its plot in Figure 6(b) as well as several parts of the plot for  $\text{oct}$  in Figure 6(c) with  $\text{NaN}$  in the respective table.

The results are similar to those for Test Problem 2: `tet` fails to satisfy (5), and

the same often happens to `20near` and `oct` on less regular node sets; the error plots in Figure 6(b-d) are not always monotone, which indicates fluctuations in the stability of the system matrix; `oct-dist` belongs to best performers overall in all cases, and `pQR3` for optimized triangulations and gridded nodes. In contrast to Test Problem 2, `pQR4` does not perform well on the unoptimized triangulations until they are sufficiently fine. Note that the second order finite element method `fem2` does not seem advantageous over `fem1` for this domain, especially if the higher density of its system matrix is taken into account. Nevertheless, the slope of its error plot in Figure 6(a) indicates a higher convergence order, which presumably would make `fem2` preferable on further refined triangulations.

# $\Xi_{\text{int}}$	FEM	Polyharmonic $r^5$ with quadratic polynomial					Pivoted QR	
		fem1	tet	oct	oct-dist	20near	pQR4sel	pQR3
816	3.5e-02	NaN	3.4e-02	2.7e-02	8.8e-02	4.9e-02	2.1e-02	3.0e+00
1254	2.4e-02	NaN	2.8e-02	1.9e-02	7.6e-02	4.1e-02	1.7e-02	9.4e-02
2414	1.8e-02	NaN	2.0e-02	1.4e-02	3.6e-02	2.6e-02	1.2e-02	4.4e-02
4423	1.2e-02	NaN	1.5e-02	1.0e-02	2.5e-02	1.8e-02	9.4e-03	4.2e-02
8401	8.4e-03	NaN	1.0e-02	7.3e-03	1.8e-02	1.4e-02	6.8e-03	6.9e-03
16437	5.9e-03	NaN	7.8e-03	5.1e-03	1.2e-02	9.7e-03	4.5e-03	1.0e-02
33030	4.2e-03	NaN	6.0e-03	3.8e-03	9.6e-03	7.2e-03	3.3e-03	2.7e-03
65652	3.2e-03	NaN	4.4e-03	3.1e-03	6.3e-03	5.2e-03	2.6e-03	3.5e-03
133295	1.9e-03	NaN	2.8e-03	1.7e-03	4.6e-03	3.5e-03	1.6e-03	1.3e-03
density	14.2	14.2	16.0	12.4	18.8	18.8	9.5	18.8

Table 14: Test Problem 3: RRMS errors  $E_{\text{ref}}$  for optimized triangulations with  $H_0 = 6.8$ . Parameters of `oct-dist`:  $s = 1$ ,  $n = 3$ ,  $k = 13$ .

# $\Xi_{\text{int}}$	10268	14078	24426	40806	71249	132581	density
fem2	9.1e-03	6.5e-03	5.3e-03	3.3e-03	2.1e-03	1.3e-03	25.5

Table 15: Test Problem 3: RRMS errors  $E_{\text{ref}}$  of the quadratic finite element method for optimized triangulations with  $H_0 = 7.1$ .

# $\Xi_{\text{int}}$	FEM	Polyharmonic $r^5$ with quadratic polynomial					Pivoted QR	
		fem1	tet	oct	oct-dist	20near	pQR4sel	pQR3
553	7.9e-02	NaN	NaN	1.23e+00	NaN	1.23e-01	1.85e+00	3.04e+00
738	6.1e-02	NaN	NaN	6.95e-01	NaN	9.04e-02	2.22e-01	1.79e+00
1092	5.8e-02	NaN	NaN	5.31e-02	NaN	5.98e-02	1.30e-01	3.62e-01
1918	4.1e-02	NaN	NaN	6.30e-02	NaN	3.47e-02	1.14e-01	1.04e+01
3967	2.8e-02	NaN	NaN	1.92e-02	NaN	1.90e+05	1.06e+01	6.02e-01
7964	1.6e-02	NaN	NaN	1.37e-02	NaN	2.10e-02	1.20e-01	5.89e-02
16219	1.4e-02	NaN	NaN	7.68e-03	NaN	1.13e-02	Inf	8.26e-03
32460	6.6e-03	NaN	NaN	5.61e-03	NaN	7.74e-03	2.27e-01	1.00e-01
65240	5.7e-03	NaN	NaN	4.37e-03	NaN	5.85e-03	2.46e+06	2.25e-02
132782	5.1e-03	NaN	NaN	2.58e-03	NaN	3.82e-03	3.63e-03	1.76e-03
density	14.9	14.9	15.9	15.93	18.3	18.8	9.6	18.8

Table 16: Test Problem 3: RRMS errors  $E_{\text{ref}}$  for unoptimized triangulations. Parameters of `oct-dist`:  $s = 3$ ,  $n = 6$  and  $k = 17$ .

Triangulation	min $\gamma$	avg $\gamma$	$0 < \gamma \leq 0.25$	$0.25 < \gamma \leq 0.5$	$0.5 < \gamma \leq 0.75$	$0.75 < \gamma \leq 1.0$
Optimized	0.09	0.88	0.0%	0.1%	4.6%	95.3%
Unoptimized	1.0e-13	0.72	7.7%	8.7%	24.6%	58.9%

Table 17: Test Problem 3: Statistics of the aspect ratio  $\gamma_T$  for the simplices of the 3D triangulations used in the tests with finite element method `fem1` reported in Tables 14 and 16.

# $\Xi_{\text{int}}$	Polyharmonic $r^5$ with quadratic polynomial				Pivoted QR	
	oct	oct-dist	20near	pQR4sel	pQR3	pQR4
393	NaN	4.0e-02	1.4e-01	3.9e-02	2.7e-02	3.1e-01
805	3.7e-02	3.1e-02	1.1e-01	3.4e-01	1.5e-02	8.4e-02
1812	NaN	2.2e-02	1.2e-01	1.7e-02	1.1e-02	2.7e-02
3816	2.1e-02	1.1e-02	2.3e-02	1.1e-02	8.6e-03	6.7e-02
7507	8.8e-03	9.3e-03	2.4e-02	8.7e-03	5.5e-03	2.1e-02
16143	7.3e-03	5.5e-03	1.1e-02	5.6e-03	4.0e-03	1.8e-02
32862	5.0e-03	4.6e-03	6.6e-03	4.1e-03	2.5e-03	6.2e-03
66716	4.2e-03	2.7e-03	4.1e-03	2.7e-03	2.3e-03	9.1e-03
135410	NaN	2.7e-03	3.6e-03	1.9e-03	1.7e-03	7.7e+00
density	7.6	7.9	8.1	8.3	6.9	8.3

Table 18: Test Problem 3: RRMS error  $E_{\text{ref}}$  for uniform interior grids and boundary nodes from optimized triangulations. The 7-node grid stencil (8) is used whenever possible. Parameters of `oct-dist`:  $s = 1$ ,  $n = 3$  and  $k = 18$ .

# $\Xi_{\text{int}}$	Polyharmonic			Pivoted QR	
	oct-dist	20near	pQR4sel	pQR3	pQR4
392	2.6e-01	3.3e-01	1.3e+00	1.0e-01	3.3e-01
862	1.9e-01	2.8e-01	1.1e-01	5.3e-01	3.7e-01
1819	1.9e-02	5.4e-02	5.1e-02	2.0e-01	1.5e+00
3808	6.2e-02	6.1e-02	1.3e-01	6.2e-02	8.9e-01
7886	3.1e-02	2.4e-02	1.1e-02	2.6e-02	1.6e+00
16181	6.3e-03	7.9e-03	5.4e-03	2.2e-02	2.9e-01
33076	3.1e-03	4.1e-03	3.4e-03	3.9e-03	3.4e-02
67148	2.5e-03	7.9e-02	3.1e-03	3.7e-02	3.5e-01
135971	1.9e-02	3.3e-03	2.1e-03	2.1e+00	2.1e-02
density	16.4	18.9	19.0	9.6	19.0

Table 19: Test Problem 3: RRMS error  $E_{\text{ref}}$  for Halton interior nodes and projected boundary nodes. Parameters of `oct-dist`:  $s = 1$ ,  $n = 3$  and  $k = 17$ .

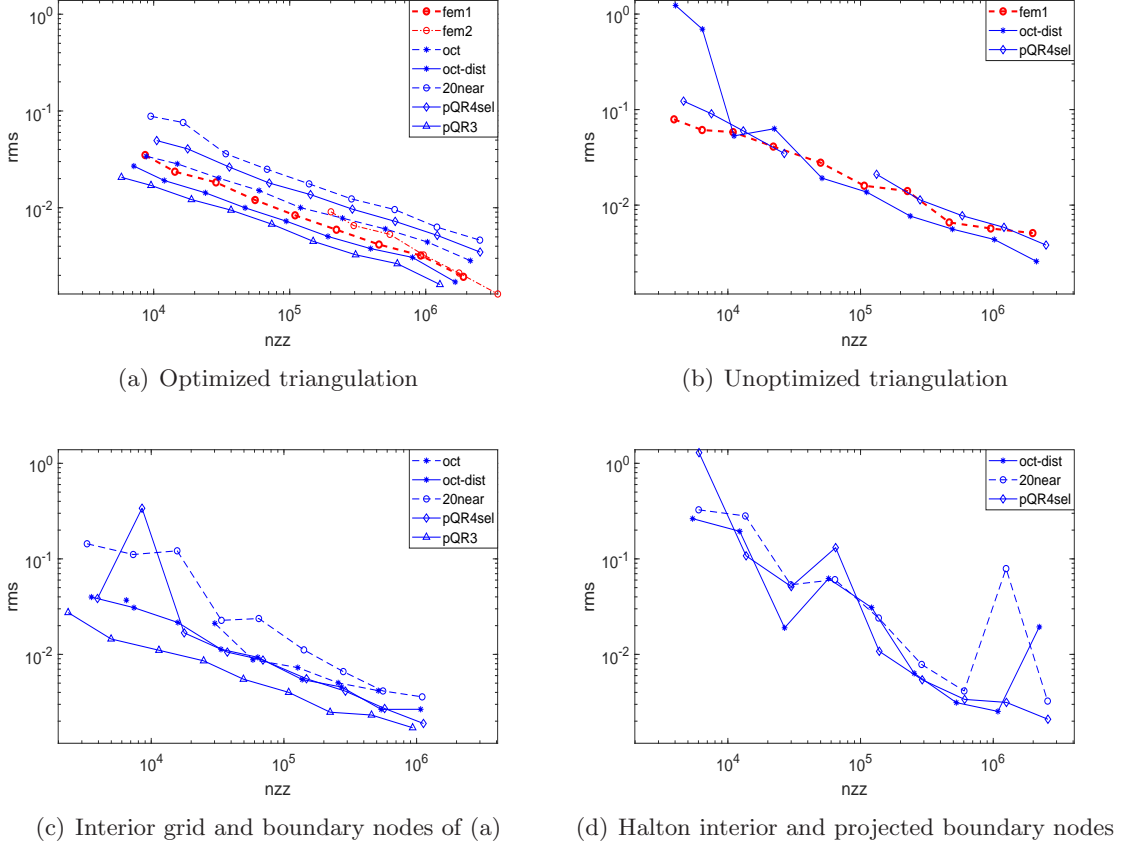


Figure 6: Test Problem 3: RMS errors as functions of  $\text{nnz}$  for meshless FD method with various versions of stencil selection, and finite element method. (a) Tables 14 and 15; (b) Table 16; (c) Table 18; (d) Table 19.

**Test Problem 4 (BeamTrussJunction).** Poisson equation  $\Delta u = -10$  with zero Dirichlet boundary conditions on the domain  $\Omega$  defined in the STL model “Beam Truss Cross and T Junction 134” designed by akerStudio, available from the platform Cults at the link <https://cults3d.com/en/3d-model/various/beam-truss-cross-and-t-junction-134>. The domain is visualized in Figure 7.

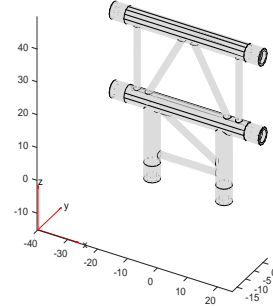


Figure 7: Test Problem 4: Domain `BeamTrussJunction` visualized by MATLAB PDE Toolbox command `pdegplot`.

A reference solution is computed by the second order finite element method on a triangulation with 1337199 nodes obtained by `generateMesh` with `Hmax = 0.3`, `Hmin = Hmax/3`, `Hgrad=1.5` and `GeometricOrder=2`.

We run the same type of experiments as for Test Problem 3. The results are reported in Tables 20–25 and Figure 8. We use  $\delta = 0.7$  for `oct-dist`, with other parameters  $s, n, k$  provided in the captions of respective tables. The results confirm the same observations made on Test Problems 2 and 3. Remarkably, the errors of `fem2` are now significantly higher than those of `fem1` and of several mFD methods despite its higher density of the system matrix. We still expect it would outperform them on denser node sets thanks to its higher order. However, assuming that the accuracy seen in the tables, e.g. the RRMS error of  $10^{-2}$ , is sufficient for an application, there seems to be no point in using a higher order method that achieves a desired error threshold with many more degrees of freedom.

### Summary observations

1. Low order meshless finite difference methods with appropriate selection of the influence sets compete well on presented test problems with the finite element method based on piecewise linear shape functions.
2. Existence of a shape regular triangulation of the nodes in  $\Xi$  does not seem to be of importance for the mFD methods. This was clearly observed for Test Problem 1. In other test problems the performance of mFD on unoptimized triangulations was significantly worse, which may be attributed to other factors such as specific features of the triangulation algorithms applied to the STL geometry, see a discussion for Test Problem 2.

# $\Xi_{\text{int}}$	FEM	Polyharmonic $r^5$ with quadratic polynomial					Pivoted QR	
		fem1	tet	oct	oct-dist	20near	pQR4sel	pQR3
538	6.8e-02	NaN	NaN	1.2e-01	1.5e-01	5.3e-02	5.3e-02	2.1e-01
664	6.7e-02	NaN	4.2e-02	4.2e-02	1.1e-01	4.9e-02	3.7e-02	9.7e-02
760	5.6e-02	NaN	3.8e-02	3.4e-02	1.1e-01	4.9e-02	3.2e-02	6.6e-02
1177	4.7e-02	2.9e-02	3.9e-02	3.0e-02	9.3e-02	4.4e-02	2.9e-02	4.0e-02
2122	3.2e-02	2.1e-02	3.6e-02	2.4e-02	7.9e-02	3.5e-02	2.5e-02	2.3e-02
3421	2.3e-02	1.7e-02	3.2e-02	1.7e-02	7.3e-02	2.9e-02	1.9e-02	1.5e-02
7101	1.7e-02	NaN	2.6e-02	1.4e-02	5.0e-02	2.5e-02	1.4e-02	1.2e-02
14798	1.2e-02	1.1e-02	1.7e-02	1.1e-02	3.6e-02	1.8e-02	1.1e-02	8.6e-03
32246	8.8e-03	NaN	1.5e-02	7.9e-03	2.5e-02	1.5e-02	8.2e-03	6.4e-03
67566	6.8e-03	NaN	1.1e-02	6.4e-03	1.9e-02	1.0e-02	6.7e-03	5.8e-03
138312	4.9e-03	NaN	8.2e-03	4.7e-03	1.1e-02	8.4e-03	4.7e-03	3.8e-03
density	13.9	13.9	15.6	12.2	18.4	18.4	9.3	18.4

Table 20: Test Problem 4: RRMS errors  $E_{\text{ref}}$  for optimized triangulations with  $H_0 = 3.0$ . Parameters of `oct-dist`:  $s = 1$ ,  $n = 3$ ,  $k = 13$ .

# $\Xi_{\text{int}}$	8809	10518	11200	15396	24735	35879	69018	135949	density
fem2	6.4e-02	4.7e-02	5.4e-02	3.8e-02	2.8e-02	2.4e-02	1.2e-02	7.2e-03	24.9

Table 21: Test Problem 4: RRMS errors  $E_{\text{ref}}$  of the quadratic finite element method for optimized triangulations with  $H_0 = 3.0$ .

# $\Xi_{\text{int}}$	FEM	Polyharmonic $r^5$ with quadratic polynomial					Pivoted QR	
		fem1	tet	oct	oct-dist	20near	pQR4sel	pQR3
876	5.0e-02	NaN	NaN	4.5e-02	1.0e+00	5.4e-02	1.5e-01	9.9e-02
1852	3.7e-02	NaN	NaN	4.4e-02	2.4e-01	5.2e-02	2.6e+01	2.6e-02
3483	3.1e-02	NaN	NaN	3.4e-02	2.6e-01	4.0e-02	4.4e-01	1.9e-02
7137	2.8e-02	NaN	3.3e-02	2.6e-02	9.8e-02	3.2e-02	3.5e-02	2.3e-02
15226	1.6e-02	NaN	2.3e-02	1.9e-02	6.7e-02	2.4e-02	1.5e-02	1.1e-02
31609	1.3e-02	2.9e-02	1.7e-02	1.5e-02	4.7e-02	1.9e-02	9.7e-03	9.5e-03
66627	1.0e-02	NaN	NaN	1.1e-02	3.1e-02	1.4e-02	7.4e-03	6.8e-03
137521	7.5e-03	NaN	9.2e-03	8.3e-03	2.1e-02	1.0e-02	6.0e-03	5.4e-03
density	14.6	14.6	15.5	15.5	17.7	18.3	9.4	18.3

Table 22: Test Problem 4: RRMS errors  $E_{\text{ref}}$  for unoptimized triangulations with  $H_0 = 1.5/2^{1/3}$ . Parameters of `oct-dist`:  $s = 3$ ,  $n = 6$  and  $k = 17$ .

Triangulation	min $\gamma$	avg $\gamma$	0 < $\gamma \leq 0.25$	0.25 < $\gamma \leq 0.5$	0.5 < $\gamma \leq 0.75$	0.75 < $\gamma \leq 1.0$
Optimized	0.43	0.88	0.0%	0.0%	6.0%	94.0%
Unoptimized	1.2e-05	0.75	3.6%	7.3%	28.1%	61.0%

Table 23: Test Problem 4: Statistics of the aspect ratio  $\gamma_T$  for the simplices of the 3D triangulations used in the tests with finite element method `fem1` reported in Tables 20 and 22.

# $\Xi_{\text{int}}$	Polyharmonic $r^5$ with quadratic polynomial				Pivoted QR	
	oct	oct-dist	20near	pQR4sel	pQR3	pQR4
815	5.6e-02	5.1e-02	1.9e-01	5.0e-02	4.6e-02	8.4e-01
1947	4.2e-02	4.0e-02	7.0e-02	3.3e-02	2.9e-02	3.2e-01
3858	2.6e-02	2.2e-02	5.0e-02	2.4e-02	1.8e-02	6.8e-02
8239	2.6e-02	1.7e-02	3.0e-02	1.8e-02	1.5e-02	2.0e-01
16386	1.9e-02	1.4e-02	2.1e-02	1.4e-02	1.1e-02	1.3e-01
35635	1.3e-02	1.0e-02	1.4e-02	9.4e-03	7.3e-03	4.1e-02
71294	9.2e-03	7.2e-03	9.9e-03	6.1e-03	6.0e-03	6.9e-01
147878	6.1e-03	5.1e-03	5.8e-03	5.2e-03	5.4e-03	2.3e-02
density	7.7	8.2	8.4	8.7	6.8	8.7

Table 24: Test Problem 4: RRMS error  $E_{\text{ref}}$  for uniform interior grids and boundary nodes from optimized triangulations. The 7-node grid stencil (8) is used whenever possible. Parameters of **oct-dist**:  $s = 1$ ,  $n = 3$  and  $k = 18$ . We start with  $h = 0.9 \text{ Hmax}$  for  $\text{Hmax} = H_0/2$  (that is,  $i = 3$ ) since larger  $h$  led to sets  $\Xi$  with too few nodes.

# $\Xi_{\text{int}}$	Polyharmonic			Pivoted QR	
	oct-dist	20near	pQR4sel	pQR3	pQR4
74	1.8e+01	8.1e-01	3.3e-01	1.9e+00	9.8e-01
174	1.1e+00	1.5e+00	7.5e-01	8.7e-01	7.5e+00
384	2.3e-01	3.8e-01	2.6e-01	9.0e-01	1.7e+00
850	2.0e-01	2.1e+00	7.9e-01	9.1e-01	5.3e+00
1828	1.4e-01	2.9e-01	5.8e-01	8.6e-01	3.5e+00
3926	1.0e-01	1.5e-01	3.8e+00	1.1e-01	4.4e-01
8238	5.9e-01	5.6e-02	9.1e-01	1.5e-01	2.2e+00
17053	1.6e-02	3.8e-02	1.6e-02	5.3e-02	2.8e-01
35193	1.1e-02	2.2e-02	2.0e-02	5.4e-02	2.0e-01
72136	1.4e-02	1.8e-02	2.4e-02	5.4e-02	1.0e-01
146898	5.6e-03	5.6e-02	2.9e-02	7.0e-02	5.0e-01
density	16.1	18.4	18.6	9.4	18.6

Table 25: Test Problem 4: RRMS error  $E_{\text{ref}}$  for Halton interior nodes and projected boundary nodes. Parameters of **oct-dist**:  $s = 1$ ,  $n = 3$  and  $k = 17$ . We skip node sets with  $0 \leq i \leq 2$ .

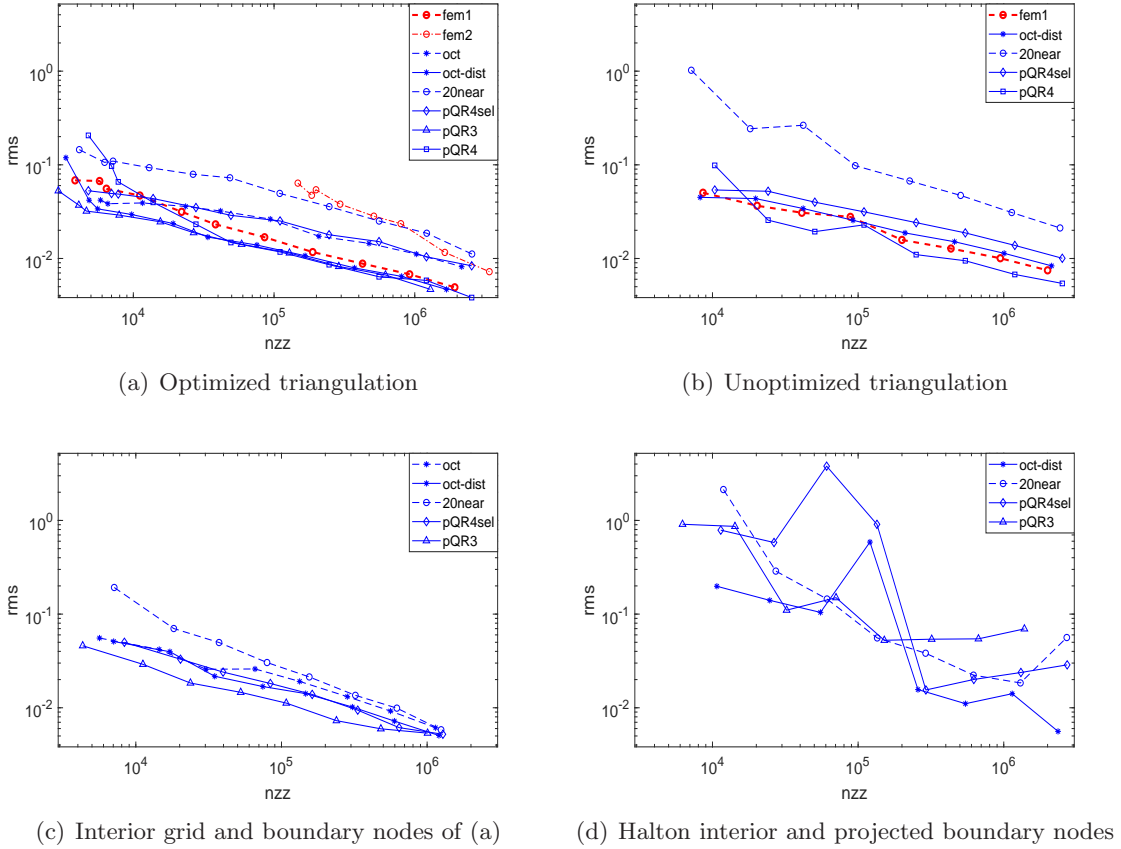


Figure 8: Test Problem 4: RMS errors as functions of  $\text{nnz}$  for meshless FD method with various versions of stencil selection, and finite element method. (a) Tables 20 and 21; (b) Table 22; (c) Table 24; (d) Table 25

3. A good discretization of the boundary was important for a good performance of mFD on the non-convex domains defined by STL models. The best node generation methods in our experiments used boundary nodes given by the vertices of an optimized triangulation. For interior nodes a rather cheap but well performing alternative to an optimized 3D triangulation was to simply take the nodes of a Cartesian grid, which also has the advantage of particularly low density of the system matrix, and provides for the possibility of using classical finite difference 7-point stencil for most interior nodes.
4. Nevertheless, all node generation methods, even the most careless, may lead to good results of mFD if the influence sets are well selected.
5. Stability constant  $\sigma$  investigated in detail for Test Problem 2 seems to be a good predictor of the performance of the mFD methods as long as the influence sets admit polynomially exact weights (5). For node discretizations  $\Xi$  generated with little care even the most reliable methods `oct-dist` and `pQR4sel` are not free from occasional spikes of the stability constant that are difficult to predict, but at least they can be detected if  $\sigma$  is computed.

6. We cannot recommend selection method `tet` as it often fails to produce sets of influence admitting polynomially exact formulas.
7. The method `oct` is significantly outperformed by `oct-dist`, whose moderate additional cost is therefore fully justified.
8. Methods relying solely on nearest neighbors are not among the best, in particular `20near` has the highest error on the optimized triangulation in all STL examples, and often fails on less regular nodes such as vertices of unoptimized triangulations. Further increasing the number of neighbors does not help, as has been demonstrated for Test Problem 2.
9. Our new `oct-dist` method is the best all-round performer among considered selection methods, even if it is often slightly outperformed by `pQR3` on more regular node sets or grids. Another method deserving attention is `pQR4sel`, which is rather robust on all types of nodes, albeit not as much as `oct-dist`, and typically leads to higher errors.
10. One of the features of `oct-dist` is that its parameters may be adjusted to particular types of problems and node distributions. In particular, we used  $\delta = 0.9$  for Test Problems 1 and 2, and  $\delta = 0.7$  for Test Problems 3 and 4 with their more complicated shapes. Parameters  $s, n, k$  were adjusted according to the type of nodes. For the nodes of unoptimized triangulations of STL models we set  $s = 3$ ,  $n = 6$ ,  $k = 17$ , and in all other cases  $s = 1$ ,  $n = 3$ , with  $k$  chosen as follows. We used  $k = 13$  for optimized triangulations except of Test Problem 1 with smooth solution on the ball, where  $k = 17$  was a better choice. For Cartesian grids we take  $k = 18$ , and for Halton nodes  $k = 17$ .

## 6 Conclusion

We have introduced a new selection algorithm `oct-dist` for the Laplace operator in 3D that works reliably with low order RBF-FD on typical STL models. In particular, cheap unoptimized 3D triangulations as well as Cartesian grids or Halton points may be employed for discretization. More regular nodes obtained by optimized triangulations are beneficial but more costly to obtain. For optimized triangulations and on grids pQR methods may be preferable.

For higher order methods the idea of the method `pQR4sel`, a combination of pQR selection with a lower order polyharmonic RBF-FD weights may be useful. Although this method was inferior to `oct-dist` in our experiments, it is easy to generalize to higher order, in contrast to `oct-dist`.

We have seen that any stencil selection method may fail to produce a stable system matrix in certain situations, hence we need a better understanding what conditions the sets of influence must satisfy in order to generate a good system matrix. We hope that practical conditions of this type will be found in the course of the research on error bounds, see [3, 22] for recent results that go beyond standard M-matrix arguments, and help to improve stencil selection algorithms.

Further experiments and possibly improvements of the selection algorithms may be needed for practical applications, involving in particular more challenging PDEs and

more complicated CAD models, for which manual interventions in the mesh generation process may be required for good results with the finite element or finite volume methods.

Successful experiments with the Cartesian grid in this paper and in [8] indicate that it is beneficial to use it as much as possible, and a promising way of node generation may include combinations of Cartesian grids of various density with local improvement of regularity of nodes in places where they meet and near boundaries and interfaces. Our experiments suggest that the existence of a mesh with high quality elements is not important for a good performance of mFD, which hopefully makes node generation for mFD a significantly simpler task than mesh generation for mesh-based methods.

## References

- [1] V. Bayona, N. Flyer, B. Fornberg, and G. A. Barnett. On the role of polynomials in RBF-FD approximations: II. Numerical solution of elliptic PDEs. *Journal of Computational Physics*, 332:257 – 273, 2017.
- [2] M. D. Buhmann. *Radial Basis Functions*. Cambridge University Press, New York, NY, USA, 2003.
- [3] O. Davydov. Error bounds for a least squares meshless finite difference method on closed manifolds, arXiv:1910.03359v1, 2019.
- [4] O. Davydov. Selection of sparse sets of influence for meshless finite difference methods, arXiv:1908.01567v1, 2019.
- [5] O. Davydov. Approximation with conditionally positive definite kernels on deficient sets. In M. N. Gregory E. Fasshauer and L. L. Schumaker, editors, *Approximation Theory XVI: Nashville 2019*, pages 27–38. Springer Berlin Heidelberg, 2021.
- [6] O. Davydov and D. T. Oanh. Adaptive meshless centres and RBF stencils for Poisson equation. *J. Comput. Phys.*, 230:287–304, 2011.
- [7] O. Davydov, D. T. Oanh, and N. M. Tuong. Octant-based stencil selection for meshless finite difference methods in 3D. *Vietnam Journal of Mathematics.*, 48:93–106, 2020.
- [8] O. Davydov and M. Safarpoor. A meshless finite difference method for elliptic interface problems based on pivoted QR decomposition. *Applied Numerical Mathematics*, 161:489–509, 2021.
- [9] O. Davydov and R. Schaback. Error bounds for kernel-based numerical differentiation. *Numerische Mathematik*, 132(2):243–269, 2016.
- [10] O. Davydov and R. Schaback. Minimal numerical differentiation formulas. *Numerische Mathematik*, 140(3):555–592, 2018.
- [11] O. Davydov and R. Schaback. Optimal stencils in Sobolev spaces. *IMA Journal of Numerical Analysis*, 39(1):398–422, 2019.
- [12] G. F. Fasshauer. *Meshfree Approximation Methods with MATLAB*. World Scientific Publishing Co., Inc., River Edge, NJ, USA, 2007.

- [13] B. Fornberg and N. Flyer. *A Primer on Radial Basis Functions with Applications to the Geosciences*. Society for Industrial and Applied Mathematics, Philadelphia, PA, USA, 2015.
- [14] P. J. Frey and P.-L. George. *Mesh generation: application to finite elements*. Wiley, 2008.
- [15] C. Geuzaine and J.-F. Remacle. Gmsh: A three-dimensional finite element mesh generator with built-in pre- and post-processing facilities. <http://gmsh.info/>.
- [16] C. Geuzaine and J.-F. Remacle. Gmsh: A 3-D finite element mesh generator with built-in pre-and post-processing facilities. *International journal for numerical methods in engineering*, 79(11):1309–1331, 2009.
- [17] P. S. Jensen. Finite difference techniques for variable grids. *Comput. Struct.*, 2(1-2):17–29, 1972.
- [18] T. Liszka and J. Orkisz. The finite difference method at arbitrary irregular grids and its application in applied mechanics. *Comput. Struct.*, 11:83–95, 1980.
- [19] D. T. Oanh, O. Davydov, and H. X. Phu. Adaptive RBF-FD method for elliptic problems with point singularities in 2D. *Applied Mathematics and Computation*, 313:474–497, 2017.
- [20] *Partial Differential Equation Toolbox™ User’s Guide*. The MathWorks, Inc, 2017.
- [21] R. Schaback. Error analysis of nodal meshless methods. In M. Griebel and M. A. Schweitzer, editors, *Meshfree Methods for Partial Differential Equations VIII*, pages 117–143. Springer International Publishing, 2017.
- [22] I. Tominec, E. Larsson, and A. Heryudono. A least squares radial basis function finite difference method with improved stability properties. *SIAM Journal on Scientific Computing*, 43(2):A1441–A1471, 2021.
- [23] H. Wendland. *Scattered Data Approximation*. Cambridge University Press, 2005.